RESEARCH ARTICLE

Synaptic vesicle undocking induces low-frequency depression

Melissa Silva[1], Federico F Trigo[2], Isabel Llano[1], Alain Marty[1]*

[1]Université Paris Cité, CNRS, Saints-Pères Paris Institute for the Neurosciences, Paris, France; [2]Departamento de Señalización Neuronal y Glial; Instituto de Investigaciones Biológicas Clemente Estable, Montevideo, Uruguay

eLife Assessment

This **fundamental** work substantially advances our understanding of short-term plasticity mechanisms by providing evidence for release-independent low-frequency synaptic depression that reflects a model that proposes a redistribution of vesicles within the readily releasable pool, via a reduction in docking site occupancy due to vesicle undocking. The evidence supporting this model is **convincing**, with rigorous modeling, electrophysiological data and computational analysis. The work will be of broad interest to cellular neuroscientists and synaptic physiologists.

Abstract Synaptic depression is often interpreted as reflecting depletion of the readily releasable pool (RRP) following exocytosis. Such a mechanism predicts little or no depression at low stimulation frequency, as RRP replenishment should then offset the loss of vesicles by exocytosis. Nevertheless, in several types of mammalian central synapses, repetitive presynaptic stimulation at low frequency (<5 Hz) elicits synaptic depression (low-frequency depression or LFD). In the present work, we count the number of synaptic vesicles released at individual active zones to study the RRP and its replenishment during LFD. Contrary to depletion models of synaptic depression, we find that LFD does not depend on previous SV consumption. We find that LFD displays a long recovery time course (tens of seconds) when challenged by isolated stimulations but is immediately reversed by a high-frequency train. We suggest that LFD results from undocking, a shift between two classes of synaptic vesicles organized sequentially inside the RRP (replacement vs. docked vesicles) in favor of the upstream (replacement) state. To explain the dependence of LFD recovery on stimulation frequency, we propose that, while undocking is apparent hundreds of milliseconds after a stimulation, calcium-dependent docking takes only a couple of milliseconds. Consistent with the undocking model, we find that double presynaptic stimulations alleviate LFD as they favor vesicular docking and RRP replenishment. Finally, we expand our model to explain how stimulation frequency shapes short-term synaptic depression, changing from depression at low frequency to a facilitation-depression sequence at medium- or high-frequency trains.

***For correspondence:** alain.marty@parisdescartes.fr

Competing interest: The authors declare that no competing interests exist.

Funding: See page 25

Preprint posted
15 January 2026
Sent for Review
19 December 2025
Reviewed preprint v1
07 April 2026
Reviewed preprint v2
01 September 2026
Version of Record
12 October 2026

Reviewing Editor: Henrique von Gersdorff, Oregon Health & Science University, United States

© Copyright Silva *et al*. This article is distributed under the terms of the Creative Commons Attribution License, which permits unrestricted use and redistribution provided that the original author and source are credited.

Introduction

Short-term synaptic plasticity (STP) governs changes in the amplitude of synaptic signals following recent neuronal activity. These changes are often rapid and large, and they potently shape information transfer across synapses. Two main components of STP are synaptic facilitation and synaptic depression (***Zucker and Regehr, 2002***).

Synaptic depression occurs after a burst of high-frequency presynaptic firing and associated synaptic release (***Betz, 1970***; ***del Castillo and Katz, 1954***; ***Charlton et al., 1982***). This link with previous presynaptic activity led to the view that synaptic depression is largely due to a decrease

in the size of the readily releasable pool (RRP) of synaptic vesicles (SVs), following the loss of SVs by exocytosis (**Kavalali, 2006**; **Regehr, 2012**; **Zucker and Regehr, 2002**). In addition, a number of other mechanisms, including desensitization of postsynaptic receptors (**Rossi et al., 1995**; **Trussell et al., 1993**), activation of presynaptic inhibitory receptors (**Redman and Silinsky, 1994**), decreased voltage-dependent calcium entry (**Xu and Wu, 2005**), decreased SV release probability (**Wölfel et al., 2007**; **Wu and Borst, 1999**), heterogeneous release probabilities among release sites (**Neher, 2015**; **Trommershäuser et al., 2003**), and non-linear presynaptic calcium buffers (**Bolshakov et al., 2019**), contribute to synaptic depression in various proportions depending on the preparation.

In more recent years, several studies have uncovered a form of synaptic depression that may differ from the RRP depletion pattern. In invertebrate synapses (*Aplysia* **Doussau et al., 2010**; crayfish **Silverman-Gavrila et al., 2005**), as well as in mammalian central synapses hippocampal CA3 to CA1 (**Abrahamsson et al., 2007**) and CA3–CA3 (**Saviane et al., 2002**) synapses, climbing fiber to Purkinje cell synapses (**Rudolph et al., 2011**); parallel fiber to Purkinje cell synapses (**Doussau et al., 2017**); calyx of Held (**Lin et al., 2022**; **Müller et al., 2010**), repetitive stimulation at low frequency (0.1–5 Hz) induces synaptic depression. This form of synaptic depression (low-frequency depression or LFD) does not require a previous period of intense presynaptic activity, so that it is unclear whether it can be explained by the classical RRP depletion hypothesis, or by any of the alternative mechanisms mentioned above.

Recent studies suggest that the RRP is made up of a heterogeneous group of SVs and that the relevant parameter for synaptic plasticity is not the RRP size as such, but rather the proportion between two components of the RRP (primed vs. unprimed or superprimed SVs; loosely vs. tightly docked SVs; or docked vs. replacement SVs; **Blanchard et al., 2020**; **Doussau et al., 2017**; **Eshra et al., 2021**; **Fukaya et al., 2023**; **Kim et al., 2024**; **Kobbersmed et al., 2020**; **Koppensteiner et al., 2022**; **Lin et al., 2022**; **Lin et al., 2025**; **Miki et al., 2020**; **Miki et al., 2016**; **Taschenberger et al., 2016**). These results open new perspectives for the interpretation of STP (**Neher, 2024**; **Neher and Brose, 2018**; **Pulido and Marty, 2018**; **Schmidt, 2019**; **Silva et al., 2021**).

Electron microscopy studies of hippocampal synapses in culture showed that, following a single presynaptic action potential (AP) stimulation, the distance between SVs and the active zone (AZ) membrane varies as a function of time in a complex manner (**Kusick et al., 2020**; **Ogunmowo et al., 2025**). Following the immediate loss of SVs by exocytosis, the number of SVs directly in contact with the AZ membrane rapidly increases (within ~15 ms), reflecting the movement of SVs from a cytosolic location to the membrane ('calcium-dependent docking'). Within ~100 ms, SVs move back into the cytosol ('calcium-dependent undocking'). In the following several seconds, SVs partially move forward again to the AZ membrane as the system returns to its basal state. While SV docking has been associated with facilitation (**Miki et al., 2016**; **Schmidt, 2019**; **Silva et al., 2021**), the functional role of subsequent undocking has remained unclear. Here, we explore the possibility that undocking could underlie LFD.

Testing the undocking hypothesis of LFD necessitates a functional assay of various subclasses of RRP SVs, a notoriously difficult task (**Neher, 2015**). Our laboratory has developed a method to monitor the release of individual SVs at single AZ synapses between parallel fibers (PFs) and molecular layer interneurons (MLIs) in cerebellar slices ('simple synapse recording'; **Malagon et al., 2016**). Simple synapse recording has provided models of synaptic facilitation and of high-frequency depression (HFD) based on changes in occupancy of docking sites and associated SV groups inside and outside the RRP (**Miki et al., 2016**; **Tanaka et al., 2021**; **Tran et al., 2022**). In the present work, we suggest that LFD reflects a specific SV re-equilibration inside the RRP, as well as an inhibition of SV entry into the RRP. We further propose a general model of synaptic depression that explains differences between low and high stimulation frequencies.

Results

Biphasic dependence of paired-pulse ratio on inter-stimulus interval

PF-MLI synapses are considered facilitating (**Atluri and Regehr, 1998**). In the present work, we ask whether single PF-MLI synapses may turn depressing at low frequency. Using simple synapse recordings at PF-MLI junctions, short trains of four presynaptic APs were applied at various inter-stimulus intervals (ISIs) in a scrambled order. Each train was separated from the next by a 10 s-long time interval,

considered long enough to reset the system (***Tran et al., 2023***; ***Figure 1A***). The resulting EPSCs were deconvolved using the mean quantal EPSC as a kernel to yield the numbers of released SVs per AP (s_i, where i stands for AP number; ***Malagon et al., 2016***). Results of an example experiment are shown in ***Figure 1B–C***. ***Figure 1C***, *top* shows average EPSC traces for the first AP (average s_1) and for the second AP at various ISI values. ***Figure 1C***, *bottom* shows, for each ISI, the ratio of mean released SV numbers for AP #2 over the corresponding mean for AP #1 (paired pulse ratio; PPR: blue dots; results for AP #3–4 are shown in ***Figure 1—figure supplement 1***). In this experiment, the PPR defined in this manner displayed values >1 for ISIs ranging from 10 to 100 ms, and values <1 for ISIs ranging from 200 to 1600 ms. In group results, the PPR was consistently >1 for ISI values of 100 ms or less, and <1 for ISI values of 800 or 1600 ms (***Figure 1D***). A biexponential fit to the data (red curve in ***Figure 1D***) intersected the PPR = 1 line for an ISI near 300 ms. These results show that the synapse changes from facilitating to depressing depending on the ISI. They differ from the single facilitation component previously reported for this synapse (***Atluri and Regehr, 1998***). This discrepancy presumably stems from differences in experimental conditions (room temperature, stimulation of multiple presynaptic PFs and 2 mM external Ca^{2+} concentration in the previous work, vs. near-physiological temperature, single presynaptic stimulation and 3 mM external Ca^{2+} here; see below). Here, the PPR is the sum of a fast facilitation component and of a slow depression component (PPR = 1 + A_{fast} exp(-t/ τ_{fast}) - A_{slow} exp (-t/ τ_{slow}), with A_{fast} = 0.94, τ_{fast} = 230 ms, A_{slow} = 0.30, τ_{slow} = 2100 ms).

Low-frequency depression (LFD) can be modelled as reflecting a decrease in DS occupancy but no change in RS occupancy or in IP size

We previously developed a sequential two-step model of docking at PF-MLI synapses (***Miki et al., 2018***; ***Miki et al., 2016***; ***Tran et al., 2022***; ***Figure 2A***). In this model, called replacement site/docking site (RS/DS) model hereafter, each AZ contains a fixed number of docking units (DUs), with a mean value of four DUs per AZ (***Miki et al., 2017***). Each DU comprises two SV binding sites: a DS, which is directly attached to the AZ membrane, and an associated RS. The RS can accommodate an SV regardless of whether the associated DS is occupied or not, meaning that a DU can simultaneously bind two SVs (***Silva et al., 2024***). The RRP is the sum of the SVs bound to all DUs (RS and DS) in the same AZ. High-frequency AP trains induce a flow of SVs from an upstream intermediate pool (IP) to the RRP. Once in the RRP, SVs transit from the RS to the DS, and eventually undergo exocytosis (downward red arrows in ***Figure 2A***).

The RS/DS model of ***Figure 2A*** has been used to interpret phenomena of STP during and after high-frequency AP trains. In response to stimulation at 100 or 200 Hz, the s_i plot displays an initial increase up to i=2–4, reflecting synaptic facilitation, followed by a gradual decrease reflecting synaptic depression (***Miki et al., 2016***; ***Tran et al., 2022***). According to the model, the DS occupancy, δ, increases after a stimulus over its basal value, following Ca^{2+}-dependent movement of SVs from RS to DS. This explains the initial facilitation. Subsequent synaptic depression reflects a δ decrease following the gradual exhaustion of IP SVs and consequently, a decrease in the flow of SVs into the RRP. Recovery requires the refilling of the IP, and it occurs on a time scale of hundreds of ms.

To explore the mechanisms underlying STP as a function of AP frequency, we alternated 8-AP stimulations at 100 Hz and at 2 Hz. Immediately after the 2 Hz train, we repeated the 100 Hz train, before repeating the entire protocol again after a pause of 10 s, to allow for synapse recovery (***Figure 2B***). According to our previous work (***Tran et al., 2022***) and within the framework of the RS/DS model, we can estimate the occupancy of the RRP and the intermediate pool (IP) during the low-frequency stimulation by comparing the s_i curves of the 100 Hz trains before (control) and immediately after (recovery) the 2 Hz train. Under the hypothesis that the release probability of docked vesicles (p_r) remains constant throughout the AP train, changes in δ, in RS occupancy (ρ), and in IP size are reflected by changes in the number of released SVs for AP #1 (s_1), for AP #2 (s_2), and for the average of AP #5–8 ($s_{5\text{-}8}$), respectively. This analysis was derived under conditions of elevated release probability. Therefore, in most of our experiments, we used an increased external Ca^{2+} concentration (3 mM) to facilitate the interpretation of the results in terms of changes in RRP and IP occupancy; results obtained under physiological external Ca^{2+} concentration conditions will be reported below.

The results of these experiments are shown in ***Figure 2C–E***. In keeping with the results of ***Figure 1***, when stimulating at 2 Hz in 3 mM external Ca^{2+} concentration, a clear synaptic depression was observed (PPR = 0.74 ± 0.05, paired one-tailed t-test, p=0.0027, n=7; blue traces in ***Figure 2C***; absolute SV

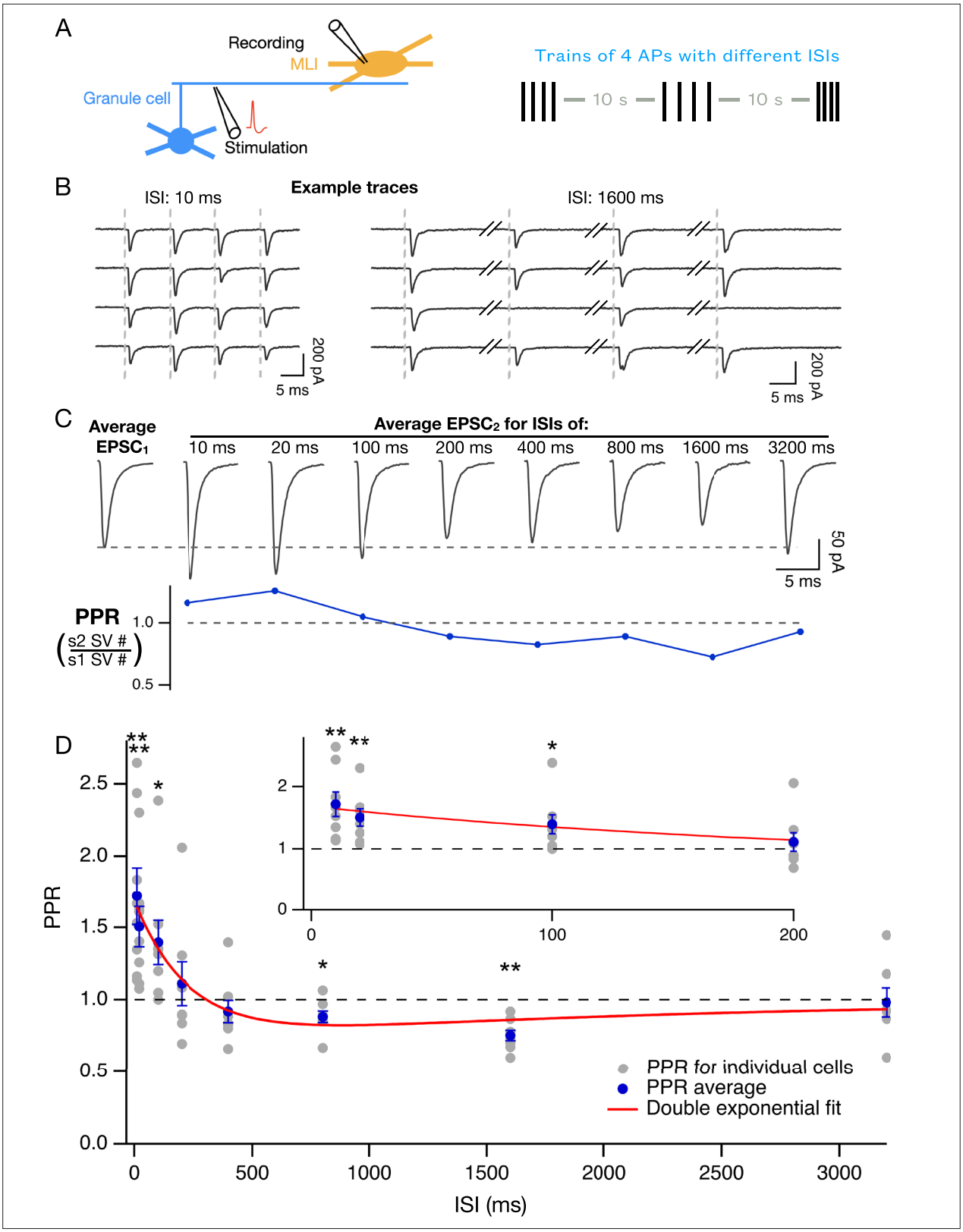


Figure 1. Dependence of paired-pulse ratio on inter-stimulus interval. (**A**) Experimental protocol. To obtain simple synapse recordings, individual granule cell axons were stimulated with an extracellular pipette located in the granule cell layer, and EPSCs were recorded in a postsynaptic MLI. Presynaptic stimulations involved trains of four APs with various inter-stimulus intervals (ISIs), and with 10 s inter-train intervals. (**B**) Example recording showing responses to trains using 10 ms ISIs (left) and 1600 ms ISIs (right). Stimulation times indicated by dotted vertical lines. (**C, Top**) Average EPSC

Figure 1 continued on next page

Figure 1 continued

in response to AP #1 (1st trace, labelled 'average EPSC1') followed by average responses to AP #2 for ISIs varying from 10 ms to 3200 ms, from the same experiment (20 repetitions for each ISI). (**C, Bottom**) A measure of the paired-pulse ratio, PPR, calculated from the ratio of the mean numbers of released SVs for AP #2 over the average release for AP #1 from the same data. Numbers of SVs released by individual presynaptic stimulations were determined by deconvolution, using the mean quantal EPSC as kernel. (**D**) Plot of PPR as a function of ISI (same analysis as in C, bottom: grey dots, individual cells (means from >20 repetitions for each cell); blue dots and associated error bars, means ± SEM from n=8 cells). The red curve is a double exponential fit to the data with A_{fast} = 0.94, τ_{fast} = 230 ms, A_{slow} = 0.30, τ_{slow} = 2100 ms. Inset: Blow-up of results for ISIs of 200 ms or less. * and ** indicate data points that differ from PPR = 1 with p<0.05 and p<0.01 respectively.

The online version of this article includes the following figure supplement(s) for figure 1:

Figure supplement 1. Trains of four successive EPSCs with different ISIs.

numbers in ***Figure 2C** top*, and values normalized to control s_1 value in ***Figure 2C** bottom*). The s_i curve for 2 Hz trains could be approximated to an exponential decay with an asymptote of 0.69±0.05 (paired one-tailed t-test, p=0.0032, n=7) and a time constant of 0.87 ISIs (435 ms; red curve in ***Figure 2C** bottom*). We then compared release during control and recovery trains to investigate the origin of the synaptic depression (***Figure 2D***). The value of s_1 at the onset of the recovery train replicated the stable low s_i values observed at the end of the low-frequency train. It displayed a decrease with respect to the s_1 value of control trains (to 70% of this control; p=0.02, one-tailed paired t-test; ***Figure 2C** bottom*). As s_1 is a proxy for δ under the present experimental conditions, this result suggests that LFD involves a decrease in δ, as previously suggested for HFD or moderate-frequency depression (***Borges-Merjane et al., 2020***; ***Lin et al., 2022***; ***Miki et al., 2016***; ***Tanaka et al., 2021***). Strikingly, s_i values during the recovery train caught up with control values immediately after the first stimulation, so that neither s_2 nor $s_{5\text{-}8}$ values differed from those of control 100 Hz trains (s_2=1.30 ± 0.09 for control and 1.16±0.10 for recovery; p>0.05; $s_{5\text{-}8}$ = 5.05 ± 0.68 for control and 5.02±0.63 for recovery; p>0.05, one-tailed paired t-test; compare yellow and black s_i curves in ***Figure 2D***; summary graph in ***Figure 2E***). Within the framework of the RS/DS model, these results suggest that neither ρ nor the IP size were decreased at the end of the low-frequency train. Taken together, the results suggest similarities and differences between the mechanisms of synaptic depression at high frequency, as studied before, and at low frequency, as studied here. In both cases, the RS/DS model suggests that synaptic depression is accompanied by a decrease in δ. However, while ρ and IP pool size accompany the δ decrease during synaptic depression at high stimulation frequency (***Tanaka et al., 2021***; ***Tran et al., 2022***), only δ is changed during LFD.

LFD as a function of stimulation frequency and external calcium concentration

Having documented LFD at 2 Hz stimulation frequency and in 3 mM external Ca^{2+} concentration as shown in ***Figure 2***, we next examined the results of similar experiments when changing the stimulation frequency to 1 Hz, or when reducing the external Ca^{2+} concentration to near physiological concentration (1.5 mM). When stimulating at 1 Hz, LFD was obtained (***Figure 2—figure supplement 1A***), blue triangles; fractional response at steady state: 0.79±0.08, paired one-tailed t-test, p=0.0037, n=5. As was the case with 2 Hz stimulations, the s_i curve recovered immediately after the first stimulus during the recovery train (yellow curves in ***Figure 2—figure supplement 1A***). Next, we examined synaptic responses at 2 Hz in 1.5 mM external calcium, finding no depression (***Figure 2—figure supplement 1B***). At this calcium concentration, synapses facilitate more than at 3 mM (compare control black normalized traces in ***Figure 2C** bottom* in 3 mM Ca^{2+}, and ***Figure 2—figure supplement 1B–C** right* in 1.5 mM Ca^{2+}), potentially causing a longer-lived facilitation that would mask the depression. To test this theory, we performed the same protocol at 0.5 Hz in 1.5 mM Ca^{2+}. While the PPR was not significantly <1 (PPR = 0.83 ± 0.11, n=6; p=0.21, paired two-tailed t-test), the rest of the train led to a reduced number of released SVs compared to control s_1 (fractional response at steady state: 0.69±0.05, n=6; p=0.00058, paired one-tailed t-test), indicating LFD. An exponential fit to the 0.5 Hz data (red curve in ***Figure 2—figure supplement 1C**, right*) indicated a τ of 1.8 stimuli (3.6 s), slower than that observed for higher calcium concentrations at 2 Hz. The recovery curve (yellow, ***Figure 2—figure supplement 1C***) showed a full recovery to control values once high-frequency stimulation was resumed.

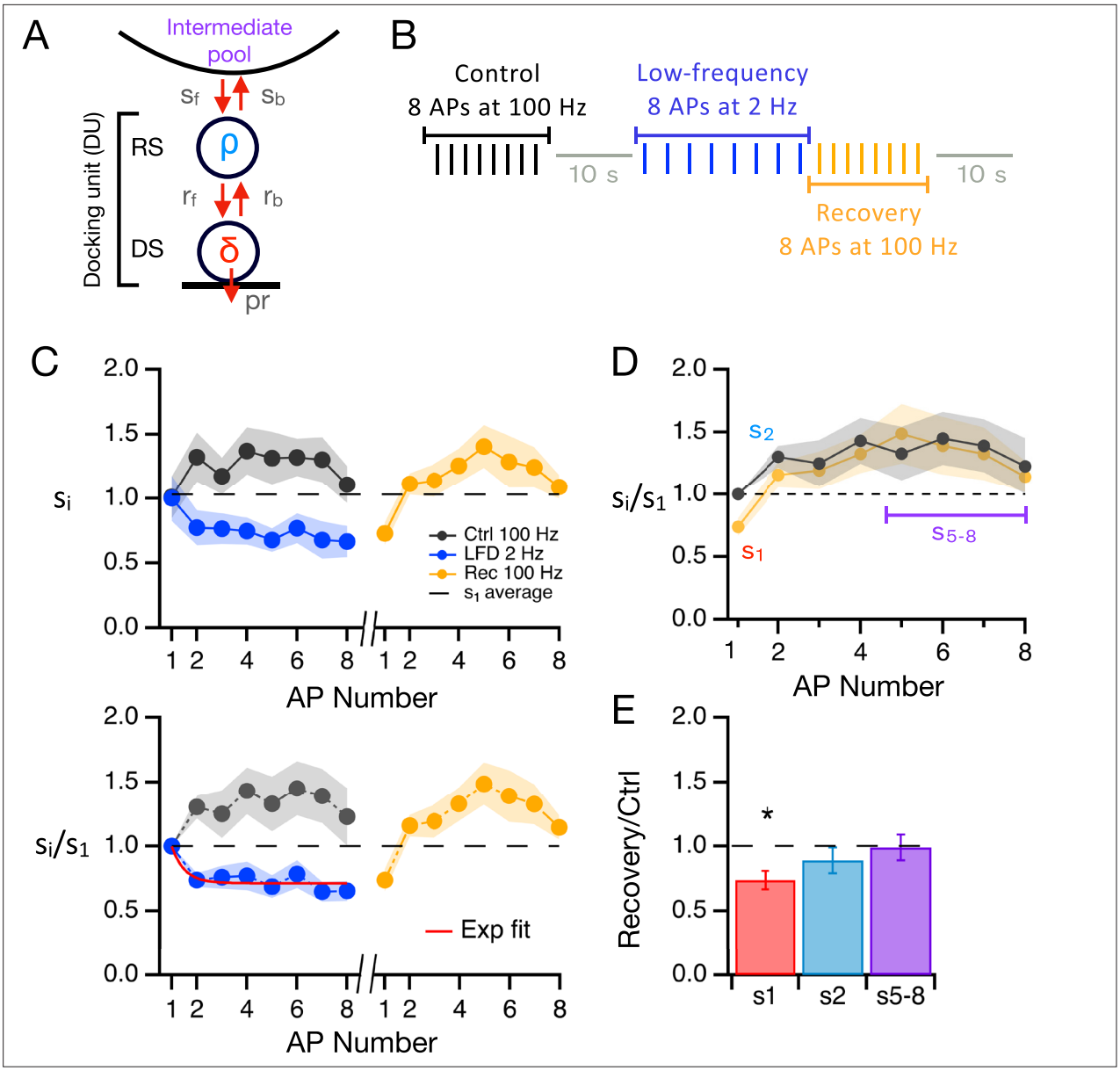


Figure 2. LFD reflects a decrease in docking site occupancy. (**A**) Sequential two-state docking model. SVs coming from the intermediate pool (IP) transit through a replacement site (RS, with occupancy ρ) and an associated docking site (DS, with occupancy δ) before release. Taken together, one RS and one DS constitute one docking unit (DU). s_f, s_b, r_f, and r_b represent transition rates as indicated. p_r represents the release probability of a docked SV following an AP. (**B**) Experimental protocol. To probe the state of SV pools in the synapse, trains of 8 APs at 100 Hz were applied either in isolation (control train), or after a depressing train of 8 APs at low stimulation frequency (recovery train). (**C, Top**) Plots (means ± SEM from n=7 cells; >20 repetitions for each cell) of s_i for the control train (black), for the low-frequency train (2 Hz, blue), and for the recovery train (yellow). Dotted line: Average s_1 value from control and low-frequency trains. (**C, Bottom**) Same, after normalization with respect to s_1 value. Exponential fit with asymptotic value = 0.69 ± 0.05 and time constant = 0.87 AP # (=435ms; red curve). (**D**) Superimposed s_i plots for control (black) and recovery (yellow). Comparison of the SV release between control and recovery trains allows us to evaluate the occupancy of the RRP and of the IP at the end of the low-frequency train. SV numbers in response to the 1st ($\mathbf{s_1}$), 2nd ($\mathbf{s_2}$), and last ($s_{5\text{-}8}$) APs respectively report changes in δ (red), in ρ (blue), and in the IP size (purple). (**E**) Ratios of s_i values between recovery 8-AP train and control train. s_1 is significantly reduced, indicating a decrease in δ, but neither s_2 nor $s_{5\text{-}8}$ are changed, indicating no change in ρ or in IP size.

The online version of this article includes the following figure supplement(s) for figure 2:

Figure supplement 1. LFD at various ISI and external calcium concentration values.

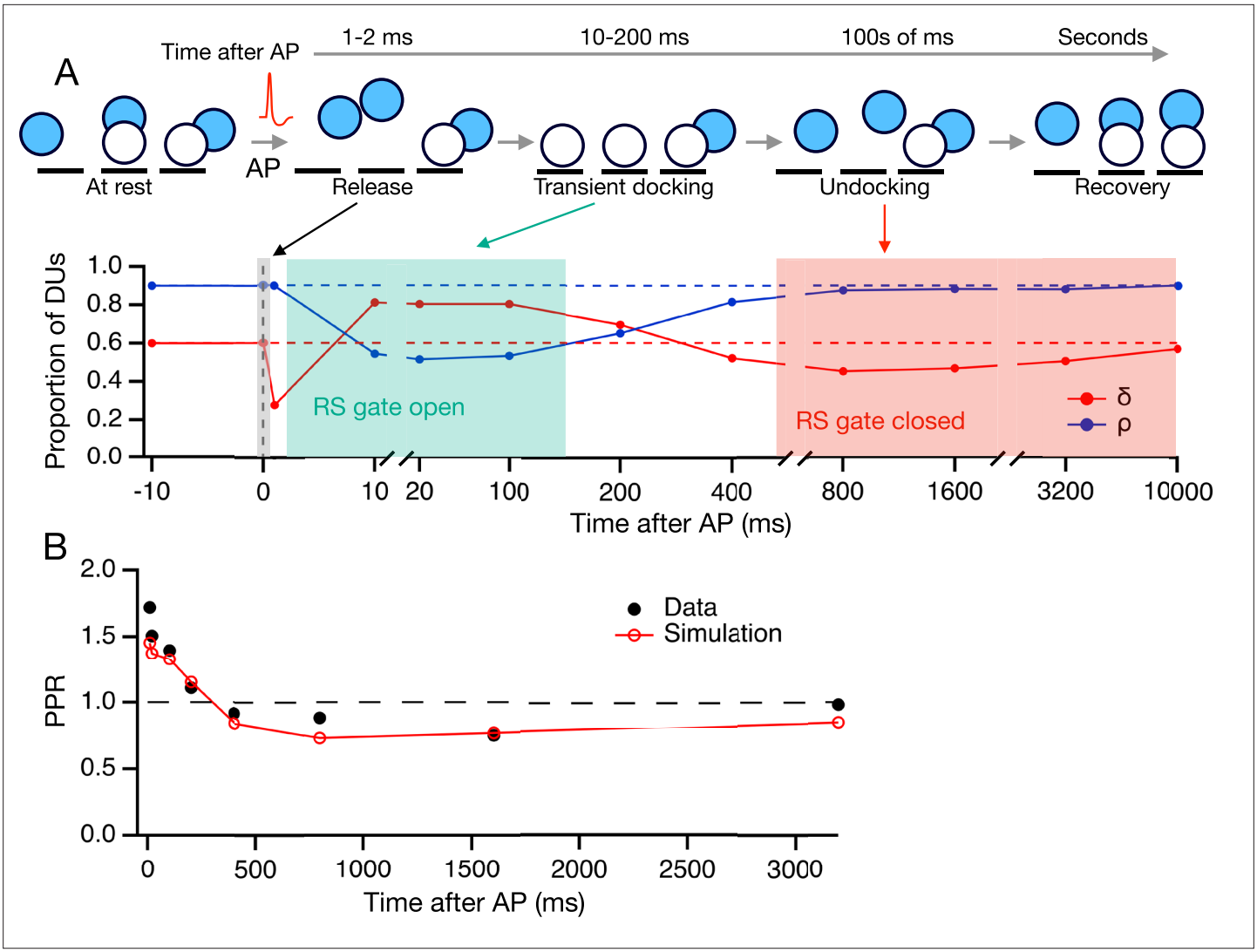


Figure 3. Simulations of s, δ, and ρ curves after an AP stimulation. (**A, up**) Model depiction of an AZ with three DUs at various time periods before and after an AP stimulation. After release, SVs transition from RS (blue; some of these SVs are placed sidewise as the two-step model cannot specify the exact location of the RS) to DS (white) within tens of ms (transient docking), then after hundreds of ms they undock, before eventually returning to their basal state. (**A, bottom**) Simulated time course of δ (red curve) and ρ (blue curve) before and after a presynaptic AP (at time 0). Resting δ and ρ values indicated by dotted lines. During transient docking, δ is high and ρ is low, so that RRP replenishment is allowed (RS gate open, green shade). During undocking, δ is low and ρ is high, so that RRP replenishment is blocked (RS gate closed, red shade). (**B**) PPR curve as a function of ISI (black dots, from ***Figure 1***) together with simulation results (red curve).

The online version of this article includes the following figure supplement(s) for figure 3:

Figure supplement 1. Time-dependent transition rates during LFD.

In conclusion, LFD can occur at 0.5, 1, or 0.5 Hz; it occurs at near-physiological external Ca^{2+} concentration (1.5 mM), but a lower frequency is required compared to 3 mM Ca^{2+} (0.5 Hz instead of 2 Hz). These experiments further confirm that LFD is immediately reversed upon stimulation with high frequency.

Modeling the dependence of PPR on ISI

The facilitation/depression curve of ***Figure 1*** matches the docking/undocking sequence reported in flash-and-freeze experiments (***Kusick et al., 2020***). Therefore, we next asked whether the RS/DS model (***Figure 2A***) could account for the dependence of the PPR on ISI on the basis of δ changes (constant p_r hypothesis). The sequence of events following an AP is shown in ***Figure 3***. Immediately after an AP, docked SVs were released with a probability p_r, resulting in a drop in δ (grey area, ***Figure 3A***).

Table 1. Kinetic parameters used in ***Figures 3 and 4***.

Simulation parameters	Figure 3	Figure 4
N	3.8	3
pr	0.55	0.55
ρ	0.9	0.9
δ	0.6	0.6
r	0.8	0.8
s	0.4	0.6
Transition probabilities	***Figure 3***	***Figure 4***
EE	0.7	0.4
EU	0.15	0.31
ED	0.15	0.29
UU	0.2	0.2
UD	0.6	0.47
UF	0.2	0.33
DD	0.7	0.4
DF	0.3	0.6

We modeled subsequent SV movements based on transition rates r_b, r_f, s_b, s_f (***Figure 2A***; ***Lin et al., 2022***; ***Miki et al., 2018***) with appropriate time-dependent changes (***Figure 3—figure supplement 1A***, ***Table 1***, and Materials and methods). This revealed a time window comprised between 10 and 200 ms when δ (red curve) was larger than its resting value of 0.6 (dotted red line, ***Figure 3A***), while ρ (blue curve) was lower than its resting value of 0.9 (dotted blue line, ***Figure 3A***). This time period corresponds with the facilitating part of the PPR vs. ISI plot (***Figure 3B***). Due to the low ρ value, SV entry into the RRP (IP to RS transition) was facilitated. We call this the 'RS gate open' configuration (green shade in ***Figure 3A***). By contrast, during the depressing part of the curve (***Figure 3B***, ISI values comprised between 500 ms and 10 s), δ was smaller than its resting value while ρ recovered near its resting value, and the 'RS gate' was closed (an SV cannot move into the RS if it is already occupied; red shade in ***Figure 3A***). The predicted PPR plot (red curve in ***Figure 3B***) is proportional to the δ curve of ***Figure 3A*** under the assumption of constant p_r. It displays a good fit to the data (black dots), showing that the model can account for the facilitation/depression sequence of ***Figure 1*** based on changes in DS occupancy.

Modeling synaptic output in response to AP trains at high or low frequency

Next, we examined whether the same model could account for the results of ***Figure 2*** (LFD for 8-AP trains and following recovery). To this end, we made concatenations of the previous model over consecutive time segments (Materials and methods). Data and simulations of 8-AP trains at high frequency (***Figure 4A***), low frequency (***Figure 4B***), and recovery trains at high frequency (***Figure 4C***) illustrate the consequences of the time-dependent changes of DU occupancy shown in ***Figure 3***. Upper panels (***Figure 4A, B and C***) show s_i plots together with simulation results, indicating that the model can reproduce the main features of ***Figure 2C*** data. Lower panels (***Figure 4A, B and C***) show plots of δ and ρ as a function of AP number. At high stimulation frequency (***Figure 4A***), δ increases and remains high throughout an 8-AP train, explaining facilitation (red curve). Meanwhile, ρ decreases below its resting level (blue curve). Because SV movement from the IP into the RRP requires a free RS, this ρ decrease facilitates RRP replenishment. In effect, the RS gate opens at AP #2 and remains open throughout the 8AP train (***Figure 4A***, *bottom*; ***Figure 4D***, *green shade*). At low stimulation frequency, a totally different pattern of changes is observed (***Figure 4B***; ***Figure 4D***, *blue shade*). δ decreases at AP #2 and remains low throughout the train, explaining LFD. ρ remains close

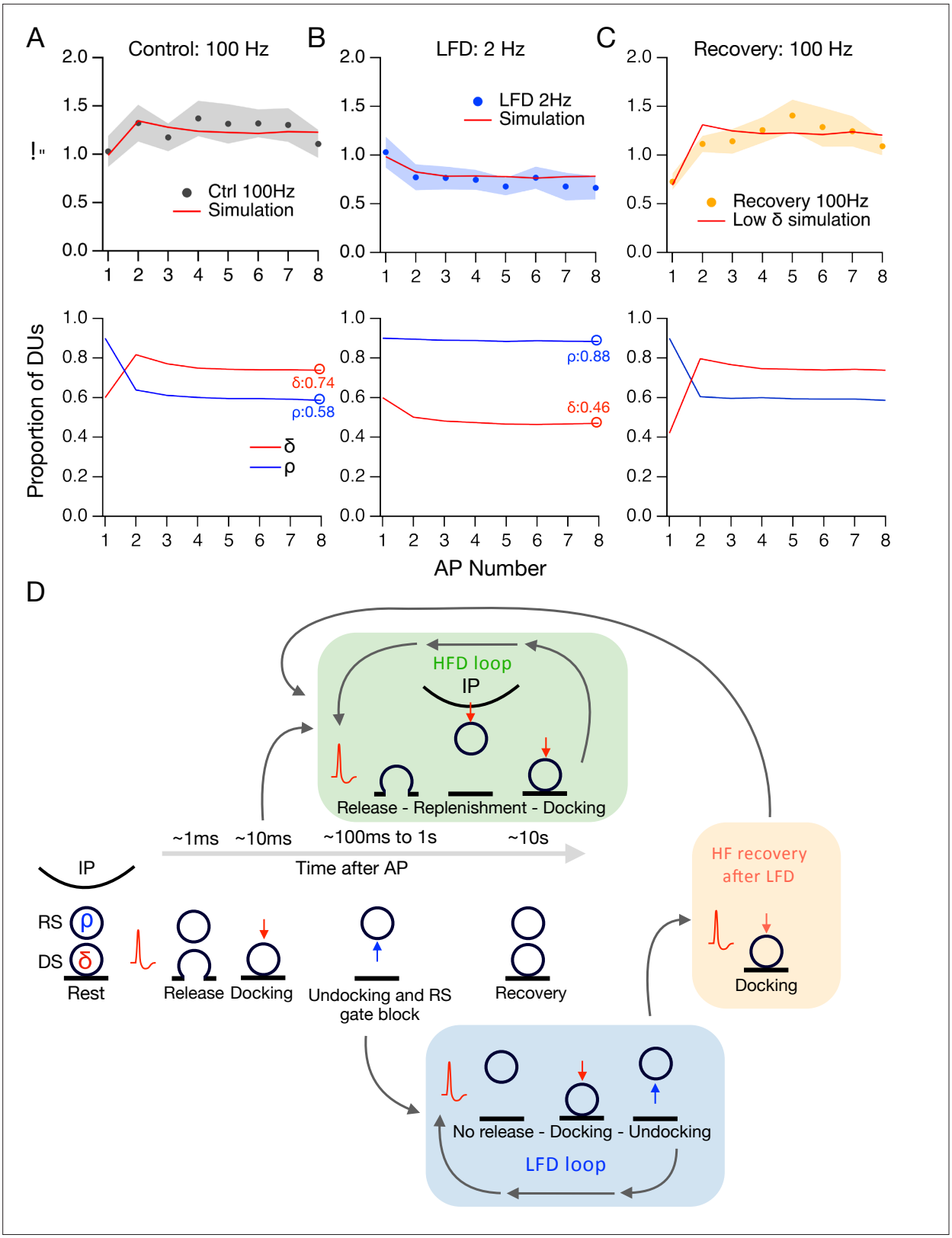


Figure 4. Simulation of SV movements during HFD and LFD. (**A, upper panel**) s_i curve during control runs with 8 APs at 100 Hz (black dots: data from ***Figure 2***; red curve: simulated results; model parameters in ***Table 1***). (**A, lower panel**) simulated values of δ (red) and ρ (blue) observed just before AP stimulations, as a function of AP #. (**B**) Same as A, but during 2 Hz 8-AP stimulations (data from ***Figure 2***). Note the behavior of δ and ρ compared to A; here ρ remains stable throughout the train, while δ undergoes a sharp initial decrease. At the end of the train, there is a low δ value and a high ρ

Figure 4 continued on next page

Figure 4 continued

value for 2 Hz trains, while at the end of a 100 Hz 8-AP train (**A**), there is a relatively high δ and a low ρ . (**C**) Same as in A, but during recovery (100 Hz; data from ***Figure 2***). The initial δ and ρ values for the recovery train simulation are the end-of-train values from the 2 Hz simulation. (**D**) Proposed SV movements during high-frequency depression (HFD) and LFD. Central sequence: proposed timeline of SV movements inside a DU following an AP stimulation. HFD loop: Proposed sequence of SV movements during HFD. The DU exits the main timeline at 10 ms after the AP to enter a loop with repetitive high-frequency AP stimulation, which results in high rates of exocytosis and RRP replenishment, as the RS gate is open (green shade). Eventually, SV depletion leads to depression. LFD loop: proposed sequence of SV movements during LFD. Here the DU exits the main timeline as the RS gate is closed, and it undergoes an idle docking-undocking cycle at each ISI (blue shade). HF recovery after LFD: Proposed sequence of SV movements during high-frequency recovery train after LFD (yellow shade). The SVs that were in the RS can dock if high frequency is applied at any point during an LFD train; if further stimuli are applied, the DU is transferred to the HFD loop (green shade) after the 2nd AP.

to its resting value of 0.9, so that the RS gate is closed before each AP of the train (***Figure 4B***, *bottom*; note that this figure shows DU parameters just before each AP, and that it does not display the time-dependent DU changes during ISIs illustrated in ***Figure 3***). These results show that both at high and at low frequency, the proportions of DU states that are reached at the end of the first ISI are kept without major changes throughout the 8-AP train.

The simulation of the recovery train used the same transition parameters as the control train. The initial ρ and δ were obtained from simulation values at the end of LFD (***Figure 4B***, *bottom*). As can be seen by comparing ***Figure 4C***, *bottom* with ***Figure 4A***, *bottom*, DUs behave identically to control from AP #2 to AP #8, in agreement with the data. Thus, our model predicts that a synapse where δ has decreased following LFD can return to its basal state within a single ISI of 10ms when challenged with a high-frequency stimulation (***Figure 4D***, *yellow shade*). If a high-frequency train is continued, the synapse enters the HFD loop (***Figure 4D***, *green shade*).

LFD does not require previous SV release events

The results and simulations of ***Figures 2–4*** suggest that LFD reflects a drop in δ, but they leave the question open as to whether the δ decrease is due to exocytosis, to SV return to RS (undocking), or to both. To better appreciate the share of each of these two mechanisms in LFD, we re-examined LFD experiments depending on the value of s_1. If s_1 is nil, the first theory predicts no synaptic depression in response to the 2nd AP, because there was no prior loss of SVs by exocytosis. Conversely, a failure of release after AP #1 should not prevent synaptic depression according to the second theory. We set aside EPSC sequences during LFD where the 1st AP resulted in release failure (s_1=0; labeled with a star in ***Figure 5A***). We pooled together results obtained with ISI values of 500, 800, and 1600 ms, as the PPR did not appear to depend on the ISI value in this range (PPR = 0.74 ± 0.05, 0.88±0.04, and 0.75±0.04 for ISIs of 500, 800, and 1600 ms respectively). We calculated separately mean s_2 values for the failure traces (noted $<s_2>|s_1=0$) as well as overall mean s_2 values (noted $<s_{2,all}>$). We obtained two separate LFD values (LFD_{fail} and LFD_{all}) by dividing $<s_2>|s_1=0$ and $<s_{2,all}>$with the overall s_1 mean, $<s_{1,all}>$. With this normalization procedure, the normalization factor was the same for successes and for failures. The two LFD values were significantly <1 (p=0.004 for LFD_{fail} and p<0.0001 for LFD_{all}, one-tailed, one-sample Wilcoxon rank test). Strikingly, we found that the two LFD values were similar (LFD_{fail} = 0.84 ± 0.05 vs LFD_{all} = 0.79 ± 0.03; p=0.24, unpaired one-tailed Wilcoxon rank test; ***Figure 5B***, *left*), indicating that the LFD value does not depend on whether the 1st AP leads to a failure or to a response.

Next, we expanded the above analysis by sorting traces displaying successful EPSCs as a function of s_1. Experimental LFD values were <1 in all cases: 0.79±0.07 for s_1=1; 0.75±0.10 for s_1=2; 0.73±0.12 for s_1 >2; respective one-tailed p values for LFD <1: 0.002, 0.01, and 0.03 (***Figure 5B***, *right*). We finally asked whether these results were compatible with our undocking model. Simulation results using the model of ***Figure 3*** gave: LFD_{fail} = 0.84; LFD_{all} = 0.73; $LFD_{s1=1}$ = 0.77; $LFD_{s1=2}$ = 0.70; $LFD_{s1>2}$ = 0.59. These values are close to experimental data (***Figure 5B***, black dots vs. bars). This agreement is remarkable since the model predicted LFD values without any parameter adjustment. Notably, the finding of identical experimental and simulated LFD_{fail} values (0.84 in both cases) is compatible with the undocking mechanism of ***Figure 3*** for LFD.

When comparing the evolution of DUs after SV release vs. after failure in the RS/DS model, it appears that the difference in DS occupancy resulting from release in the first case is compensated in a time frame on the order of 10ms due to the high value of the RS ->DS transition rate. Because of this

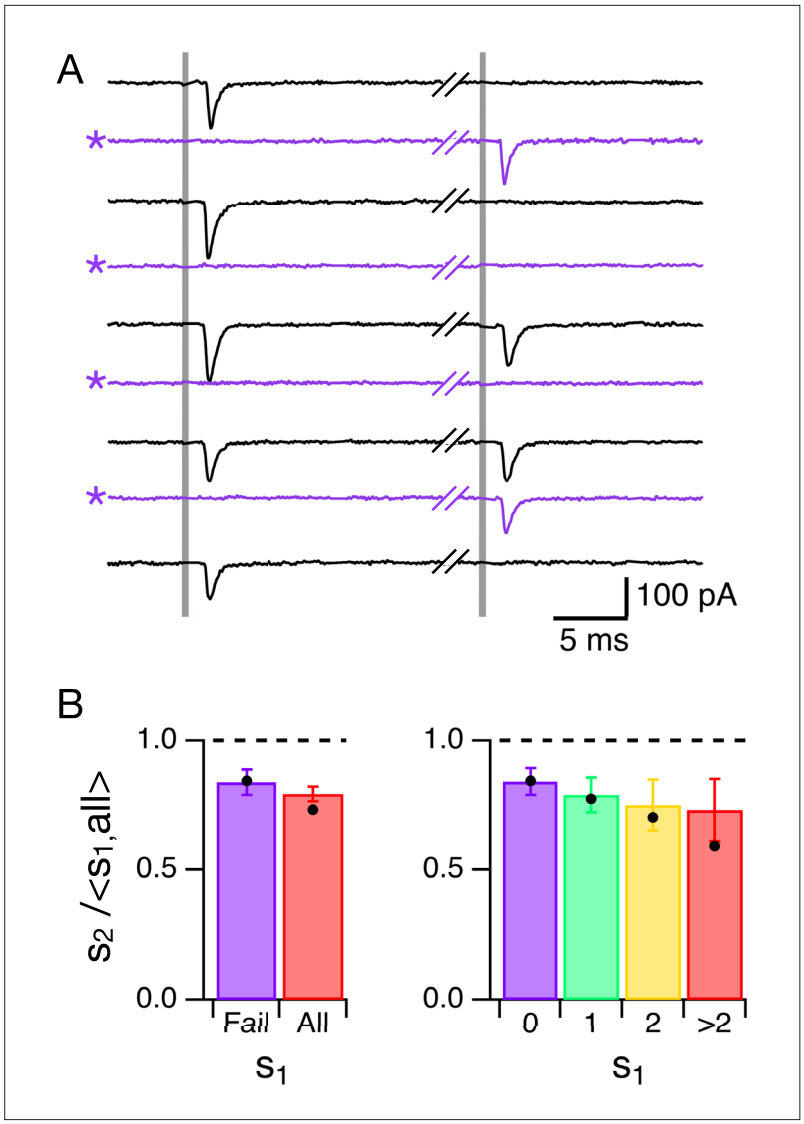


Figure 5. RRP depletion does not cause LFD. (**A**) Exemplar traces from an LFD experiment, illustrating responses to 1st and 2nd AP (AP times indicated by vertical grey lines) during low-frequency trains. Black traces show EPSCs including a success in response to the 1st AP, while purple traces (marked with a star) show EPSCs when there was a failure in response to the 1st AP. (**B, left**) Group data showing a similar extent of LFD (mean ± SEM of LFD across cells; n=7 cells for 500 ms; 8 cells for 800 and 1600 ms) when there was a failure in response to the 1st AP (purple bar; mean± SEM) compared to the corresponding data taken from all traces (red bar). The LFD value was obtained by calculating the ratio of the mean numbers of released SVs for the second AP over the average release for the first AP for all trials (failures and successes). (**B, right**) Same analysis, except that now LFD values are calculated separately for each s_1 value. Dots indicate predictions from the model of ***Figure 3***.

short recovery time, DUs that have released display very similar δ (before the 2nd AP) to those that have failed to release after the 1st AP, leading to almost identical s_2 values in the two cases.

In conclusion, the above results indicate that LFD occurs independently of the amount of SV release following AP #1. They support the hypothesis that LFD reflects a shift of SV occupancy favoring RSs over DSs (undocking), rather than RRP depletion caused by exocytosis.

Long AP trains at low frequency reveal two phases of LFD occurring on widely different time scales

Earlier studies showed a slow onset LFD during long trains at low frequency (***Abrahamsson et al., 2007***; ***Doussau et al., 2010***; ***Rudolph et al., 2011***). We therefore searched for an additional slow

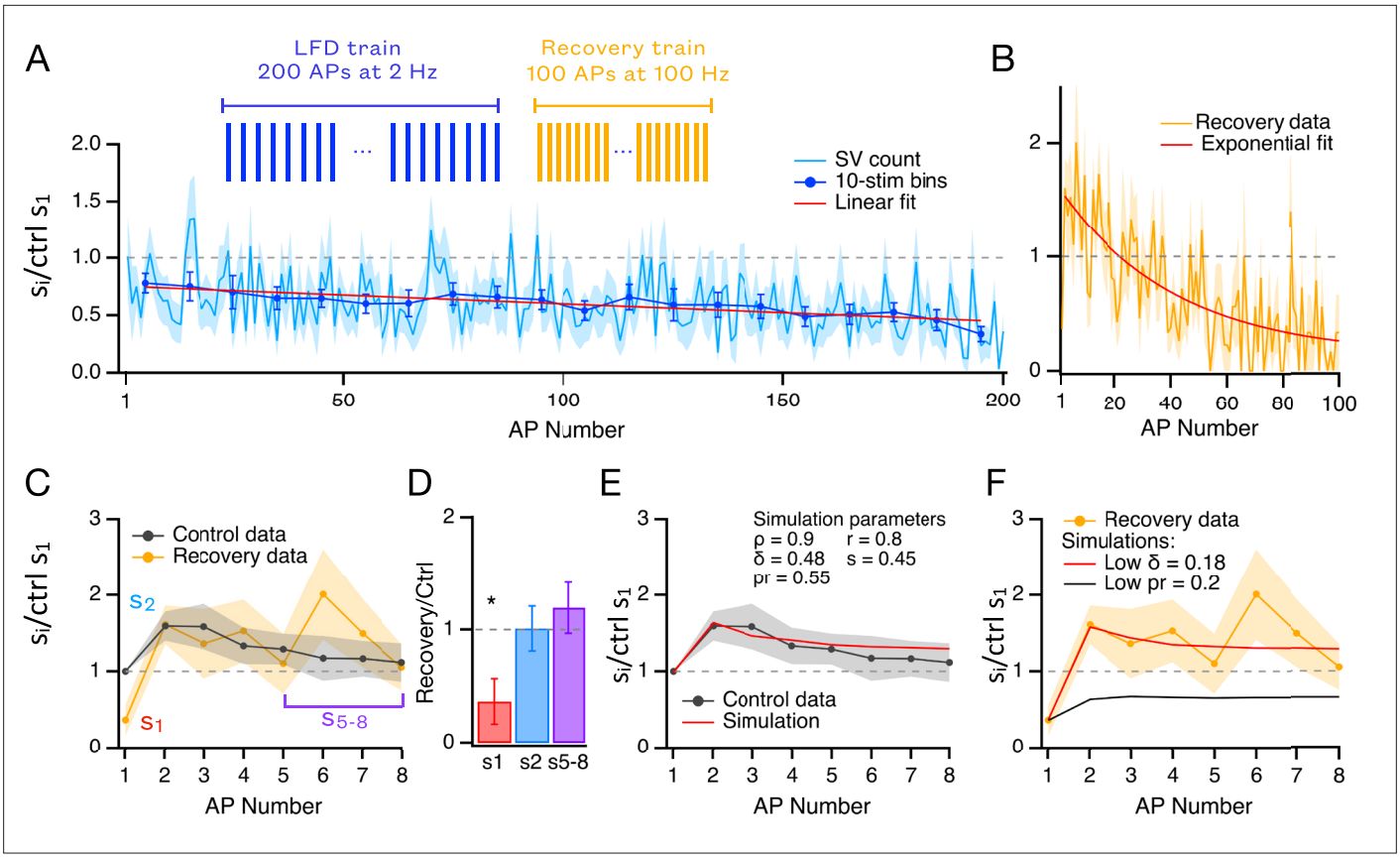


Figure 6. Prolonged low-frequency trains produce a gradual decrease in docking site occupancy. (**A**) A long AP train at low frequency (200 APs @ 2 Hz) was followed by a long recovery train (50–100 APs @ 100 Hz; experimental protocol in **insert**). Normalized plot of s_i during long low-frequency train, showing an initial rapid depression (as in ***Figure 2***, notice the reduction in release for the first binned data point) followed by a gradual depression during the entire train duration (light blue: mean ± SEM of individual trials; dark blue dots and associated error bars: binned data for 10 consecutive APs; red: linear fit to the data; n=16 trials, 8 cells). (**B**) Time course of synaptic depression during the recovery train, with exponential fit (red; time constant: 41.2 ISIs, or 412 ms). n=6 trials, 3 cells for 50 APs, 6 trials, 4 cells for 100 APs. (**C**) A series of control trains (8-APs @ 100 Hz, separated by 10 s-long inter-train intervals) were recorded before the long AP train to establish the characteristics of the synapse. Normalized s_i plots for this control and the first 8-APs of the recovery 100 Hz train are compared here. s_1, s_2, and $s_{5\text{-}8}$ are indicated in the plot. (**D**) The s_1 ratio (red) between recovery and control trains is <1, indicating a decrease in δ at the end of the low-frequency train. By contrast, neither s_2 (blue) nor $s_{5\text{-}8}$ (purple) are changed, suggesting no change in ρ or in IP size. (**E**) Simulation of control trains shown in **C** (black dots: average normalized data; red curve: simulation). (**F**) Simulation of recovery trains shown in **C** (yellow dots: average normalized data). Decreasing the release probability from p_r = 0.55 to p_r = 0.2 without changing the other simulation parameters fails to provide a satisfactory fit of recovery data (black curve), while decreasing the DS occupancy from δ=0.48 to δ=0.18 without changing the other simulation parameters provides a satisfactory fit of the recovery data (red curve).

The online version of this article includes the following figure supplement(s) for figure 6:

Figure supplement 1. Lack of recovery of LFD over tens of s after AP train.

Figure supplement 2. Binomial analysis of released SV numbers during prolonged LFD.

Figure supplement 3. Prolonged low-frequency trains with postsynaptic BAPTA.

component LFD at PF-MLI synapses. In each experiment, a series of control trains (8-APs @ 100 Hz) was presented first. Next, a long low-frequency train was applied (200 APs @ 2 Hz in ***Figure 6A***), followed by a recovery train (50 or 100 APs @ 100 Hz; ***Figure 6B***; protocol in ***Figure 6A***, inset). Numbers of released SVs per AP (s_i) were normalized with respect to the s_1 value obtained for the control trains. During the long train, a plot of the normalized s_i (indicated as s_i/ctrl s_1) vs AP # displayed an initial decrease followed by a gradual depression (***Figure 6A***). We call this initial drop and the subsequent linear decrease the first and second phase of LFD, respectively. A linear fit to these data (red line in ***Figure 6A***) indicated a first phase depression (within the first 10 APs) to 75 ± 2% of the control, consistent with the previous results obtained with paired stimulation and short train protocols (***Figures 1 and 2***). The second phase of the depression exhibited a slope of –0.15 ± 0.02% per AP,

such that the value reached for the linear fit at the end of the 200-AP train was 45% of the control. A similar LFD was seen at 1 Hz with a first phase drop to 51 ± 2% of control and a slope of –0.05 ± 0.02% reaching 40% of the control at the end of the 200-AP train (n=17 trials from six cells).

We next investigated δ, ρ and IP pool size at the end of long low-frequency trains with the previous s_1/ s_2/ s_{5-8} approach. As expected, the first response of the recovery train was severely depressed compared to s_1 of control trains (recovery s_1=37.6 ± 20.2% of control s_1), but s_i plots during control and recovery trains were indistinguishable for i values of 2 or more (s_2 ratio: 1.01±0.20; s_{5-8} ratio: 1.19±0.23; ***Figure 6C–D***), suggesting again a drop in δ without changes in either ρ or IP size.

The s_1/ s_2/ s_{5-8} analysis assumes a constant p_r. To test this hypothesis, we determined the parameters of the RS/DS model by fitting responses to control 8-AP trains (***Figure 6E***). Next, responses to the first eight APs of the recovery train were predicted by keeping all parameters the same as control except for either δ or p_r. In two different simulations, δ and p_r were determined to fit the s_1 point of the recovery curve (***Figure 6F***, red and black curves respectively). While the δ decrease prediction closely matches the data (***Figure 6F***, yellow curve), the p_r decrease prediction fails to simulate the recovery train. Altogether, these results suggest that the slow phase of LFD illustrated in ***Figure 6A***, like the rapid phase shown in ***Figure 2C***, reflects a δ decrease without significant changes in p_r, in ρ or in IP size.

In these experiments, the delay between the LFD train and the recovery train was variable. A plot of the value of s_1 for the recovery plot as a function of the time interval since the end of the LFD train is shown in ***Figure 6—figure supplement 1***. This plot shows that recovery s_1 remains depressed after rest periods of up to 1 min after the end of the LFD train. These results suggest that, while SV re-equilibration within the RRP occurs very rapidly under elevated calcium concentration, as presumably occurs during the recovery trains, they occur very slowly under resting calcium concentration.

Finally, a full recovery train (50 or 100 APs @ 100 Hz) elicited a deep synaptic depression (HFD; ***Figure 6B***), similar in extent and in time course to the depression observed for stand-alone trains at high frequency. An exponential fit to these data (red curve in ***Figure 6B***) displayed a time constant of 412 ms (41.2 x the ISI) and an asymptotic value of 13% of the control s_1 value. This type of depression, unlike LFD, was previously suggested to involve a decrease in ρ and in IP size in addition to δ (***Tran et al., 2022***).

LFD is not due to stimulation failures

One tacit assumption of our analysis so far is that LFD reflects a decreased synaptic response to presynaptic stimulations. We next asked whether LFD could instead originate in erratic stimulation failures. This possibility was plausible since the failure rate increased markedly during the second phase of LFD (***Figure 6—figure supplement 2***). To test it, we compared the changes in the distributions of released SV numbers predicted from two LFD models. In the first model, during LFD, each DU releases fewer SVs when stimulated, presumably due to a reduction in δ. In the second model, a fraction of the stimulations fails to elicit a presynaptic AP during LFD, but the probability of release for each stimulated synapse remains constant (Materials and methods). Both models were constrained to reproduce the observed mean number of failures during LFD. Observed distributions of released SV numbers during LFD were compatible with the decreased δ model but not with the stimulation failure model (***Figure 6—figure supplement 2***). We conclude that stimulation failures cannot account for LFD, consistent with the above interpretation that LFD reflects a drop in δ, as well as with previous results in other preparations (***Saviane et al., 2002***; ***Silverman-Gavrila et al., 2005***).

LFD is not blocked by postsynaptic BAPTA

At synapses between PFs and Purkinje cells, low-frequency stimulation leads to a gradual synaptic depression that has been attributed to a transsynaptic mechanism (***Casado et al., 2000***). Since the simple synapse method is based on SV counts rather than EPSC amplitude, there is no doubt that the expression of LFD at PF-MLI synapses is presynaptic. Nevertheless, as AMPAR activation elevates the postsynaptic Ca^{2+} concentration (***Soler-Llavina and Sabatini, 2006***), we included BAPTA (10 mM) in the MLI recording solution to test the possibility of a retrograde LFD mechanism that would be driven by postsynaptic Ca^{2+}. We applied a long 2 Hz train (100 APs @ 2 Hz) followed by a short 8-AP recovery train (experimental protocol in ***Figure 6—figure supplement 3***, insert). The result is very similar to ***Figure 6*** data (compare ***Figure 6—figure supplement 3*** to ***Figure 6A and C***) with a first phase drop

to 65 ± 3% of the control and a second phase slope of –0.2 ± 0.05% per AP. In this case, recovery trains were applied immediately following the LFD train (whereas waiting times of 10 s of s were included in the experiments of ***Figure 6***), and the recovery is identical to that observed in ***Figure 6C***, suggesting likewise a reduction in δ with no associated change in ρ or IP size.

The similarity of results with and without a postsynaptic calcium buffer is consistent with a purely presynaptic mechanism for LFD.

No evidence for changes in presynaptic Ca^{2+} transients during LFD

Our recovery results and simulations suggest that LFD is due to a decrease of δ, not of p_r (***Figure 6F***). In line with this notion, earlier work reported no change in Ca^{2+} transients at PF-MLI synapses for paired stimulations at short ISIs (***Brenowitz and Regehr, 2007***; ***Malagon et al., 2020***; ***Miki et al., 2016***). Nevertheless, it seemed possible that a different situation would prevail with multiple stimulations and/or at longer ISIs.

To explore potential changes of presynaptic Ca^{2+} signaling during AP trains, we preloaded individual granule cells with the calcium dye OGB-6F (1–2 mM in pipette solution; duration of preloading: 90 s; ***Rebola et al., 2019***). After allowing diffusion of the calcium dye in the axon, we imaged single PF varicosities using two-photon laser microscopy (***Figure 7A***, and Supplementary Information), and we measured Ca^{2+}-dependent changes in fluorescence during 50-AP train stimulations at 1 Hz, or 200-AP train stimulations at 2 Hz, using stimulation conditions similar to those of the simple synapse experiments of ***Figure 6***. To avoid photodamage and photobleaching, imaging was interrupted after the 5th AP in a train, and it was resumed for the last five APs of the train. Traces were averaged from three to seven trials in each varicosity to improve the signal-to-noise ratio (***Figure 7A2***). Averaged traces across varicosities revealed little changes in Ca^{2+}-dependent fluorescence transients during trains either at 1 Hz (***Figure 7B***) or at 2 Hz (***Figure 7C***). $\Delta F/F_0$ values for 10 varicosities from 8 granule cells at 1 Hz were: 19.1 ± 3.9% for the 1st AP; 20.4 ± 2.8% for the 2nd AP; 19.3 ± 2.8% for the last AP; for 9 varicosities from 6 granule cells at 2 Hz: 19.4 ± 2.9% for the 1st AP; 17.9 ± 1.6% for the 2nd AP; 16.4 ± 1.9% for the last AP; p>0.05 in 1st vs. second and first vs. last, paired comparisons at both frequencies, one-tailed Wilcoxon rank test (***Figure 7D***). These data indicate that Ca^{2+}-dependent fluorescence transients were the same, within the limits of sensitivity of our measurements, in response to the first, the second, or the last AP in a train. In the same data set, we found no difference between basal fluorescence levels at the end vs. the beginning of the trains at 1 Hz (respectively, 107±12 a.u. vs. 103±10 a.u.; p>0.05, one-tailed Wilcoxon paired rank test; black markers in ***Figure 7E1***), but we found an augmentation of basal fluorescence at the end of the trains compared to the pre-stimulation value at 2 Hz (118±10 a.u. vs. 111±9 a.u.; p=0.026, one-tailed Wilcoxon paired rank test; blue markers in ***Figure 7E1***). At 2 Hz, after the end of the train, the fluorescence trace relaxed to near its pre-stimulation value with a time constant of 750 ms, confirming that the basal Ca^{2+} concentration had increased during the train (***Figure 7E2***).

In conclusion, we find no evidence of decreased Ca^{2+} transients during trains, either at 1 Hz or at 2 Hz. This is in line with our earlier conclusion that p_r changes do not contribute strongly to LFD. We find a gradual increase of pre-stimulation Ca^{2+} concentration with 200 APs at 2 Hz, but not with 50 APs at 1 Hz. This effect may contribute to the second phase of LFD at 2 Hz.

Doublet stimulations inhibit LFD

Our model predicts a high ρ value during LFD that inhibits DU replenishment by preventing the transition from the IP to the RS (RS gate closed). We next tested the prediction that during a low-frequency train, ρ remained elevated while δ decreased (***Figure 4B***), by giving two successive stimuli with a 10ms interval instead of single stimuli (doublet stimulations; ***Figure 8A–B***). According to the s_1/ s_2/ $s_{5\text{-}8}$ analysis, while the time course of the first response, s_1, should give the evolution of δ, the time course of the second response, s_2, should give the evolution of ρ (***Tran et al., 2022***). With the same experiments, we intended to test whether doublet stimulations would open transiently the RS gate and thus interfere with the time course of LFD, as suggested by earlier work at the PF-Purkinje cell synapse (***Doussau et al., 2017***).

We performed these experiments with a longer than usual ISI (5 s) to provide ample time for SVs to equilibrate after each stimulus, either singlet or doublet. Control single AP train stimulation experiments at 0.2 Hz revealed LFD (1st phase depression: 0.75±0.11; paired one-tailed t-test, p=0.037,

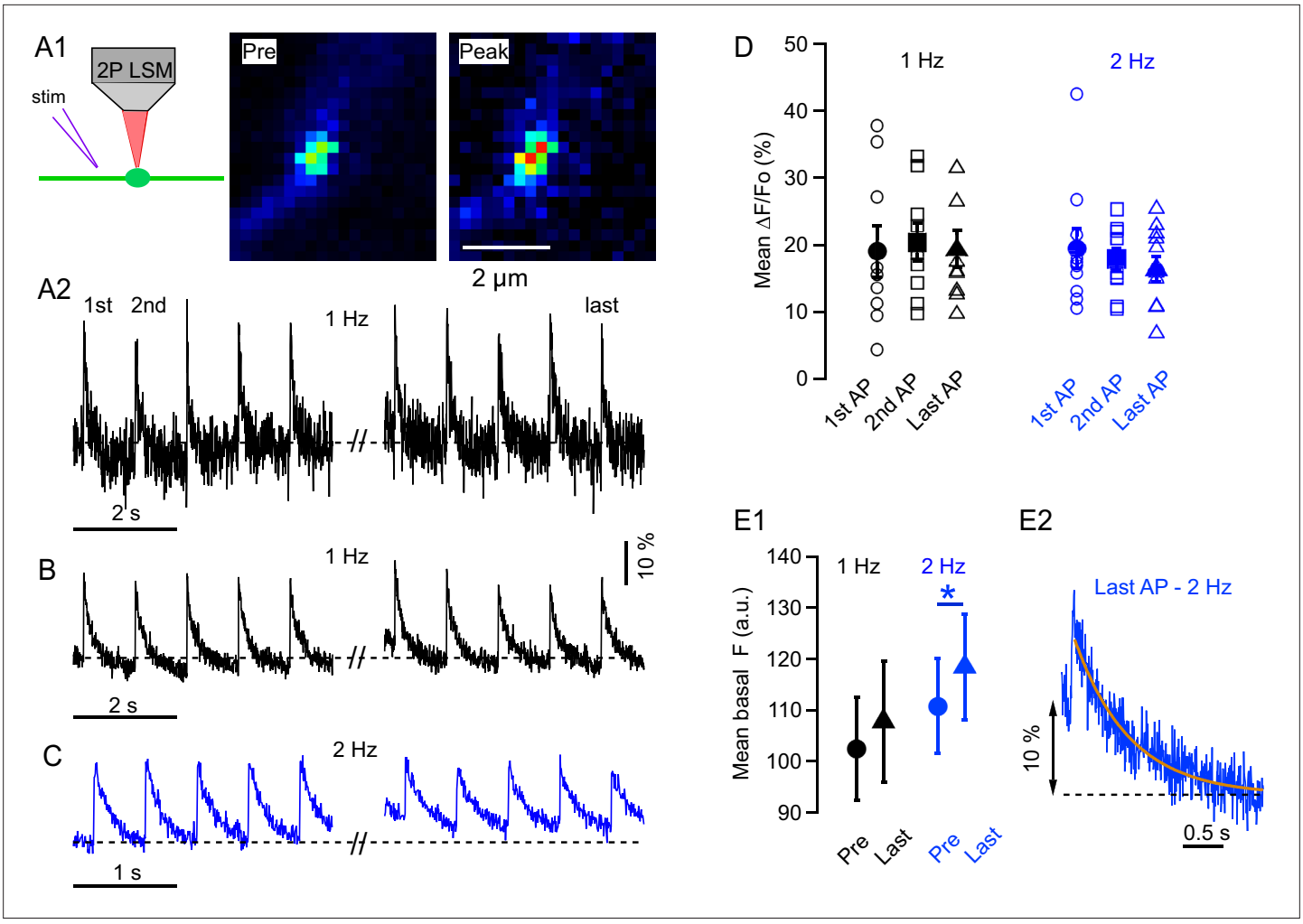


Figure 7. Presynaptic calcium transients in single PF varicosities. (**A1, left**) Diagram of the experimental recording. (**A1, center**) Image of an OGB-6F loaded PF varicosity before stimulation. (**A1, right**) Same, at the peak of the response to a single presynaptic AP. (**A2**) Average Ca^{2+}-dependent fluorescence transients ($\Delta F/F_0$ traces from n=5 trials: see Materials and methods) registered in response to the first five APs (left trace) and to the last five APs (right trace) in response to a train of 50 APs at 1 Hz, from the same varicosity as in A1. Imaging was interrupted between the two traces to avoid photodamage and photobleaching. (**B**) Average traces from a group of 10 varicosities from 8 cells at 1 Hz. (**C**) Average traces from another group of nine varicosities from six cells, in response to the first and last 5 APs from a train of 200 APs at 2 Hz. (**D**) Mean Ca^{2+}-dependent fluorescence transients (closed symbols: means across varicosities, with attached bars representing ± the SEM; open symbols: values for individual varicosities) are the same for the 1st, 2nd, and last AP in a train (left: 1 Hz stimulation; black; right: 2 Hz stimulation; blue). (**E1-E2**) Evolution of the basal fluorescence level during and after a long AP train. (**E1**) Initial and final basal fluorescence levels are not statistically different for 50 AP trains at 1 Hz (left, black), while there is a significant increase at the end of 200 AP trains at 2 Hz compared to its initial value (right, blue). (**E2**) Return of the $\Delta F/F_0$ fluorescence trace to its initial baseline (mean from five varicosities) after the end of long 2 Hz trains indicates a shift of the basal fluorescence level by 11% near the end of the train (yellow curve: exponential fit to the decay, with time constant 750ms).

n=8; exponential fit of first 12 normalized s_i points had a time constant of 3.6 ISIs, or 18 s). We then examined the extent of LFD in response to the first 20 doublet stimulations at low frequency. We found that s_1 values were reduced compared to control (normalized s_1 value during 20 first trials at 0.2 Hz: 0.80±0.10; p=0.008, two-tailed, one-sample t-test; ***Figure 8C***). These results indicate that doublet stimulations at 0.2 Hz produced significant LFD when considering the response to the 1st stimulus. By contrast, s_2 values were not affected (s_2 values normalized to control s_1: 1.18±0.11 for control 100 Hz trains; 1.11±0.10 during 20 first doublet trials; p>0.05, two-tailed, one-sample t-test; ***Figure 8C***). These results are consistent with our previous conclusion that LFD involves a decrease in δ without significant changes in ρ.

Next, we compared the plots of normalized released SV numbers as a function of AP number (i) for singlet stimulations (s_{is}; light blue), for the 1st AP of doublet stimulations (s_{id1}; dark blue), and for the

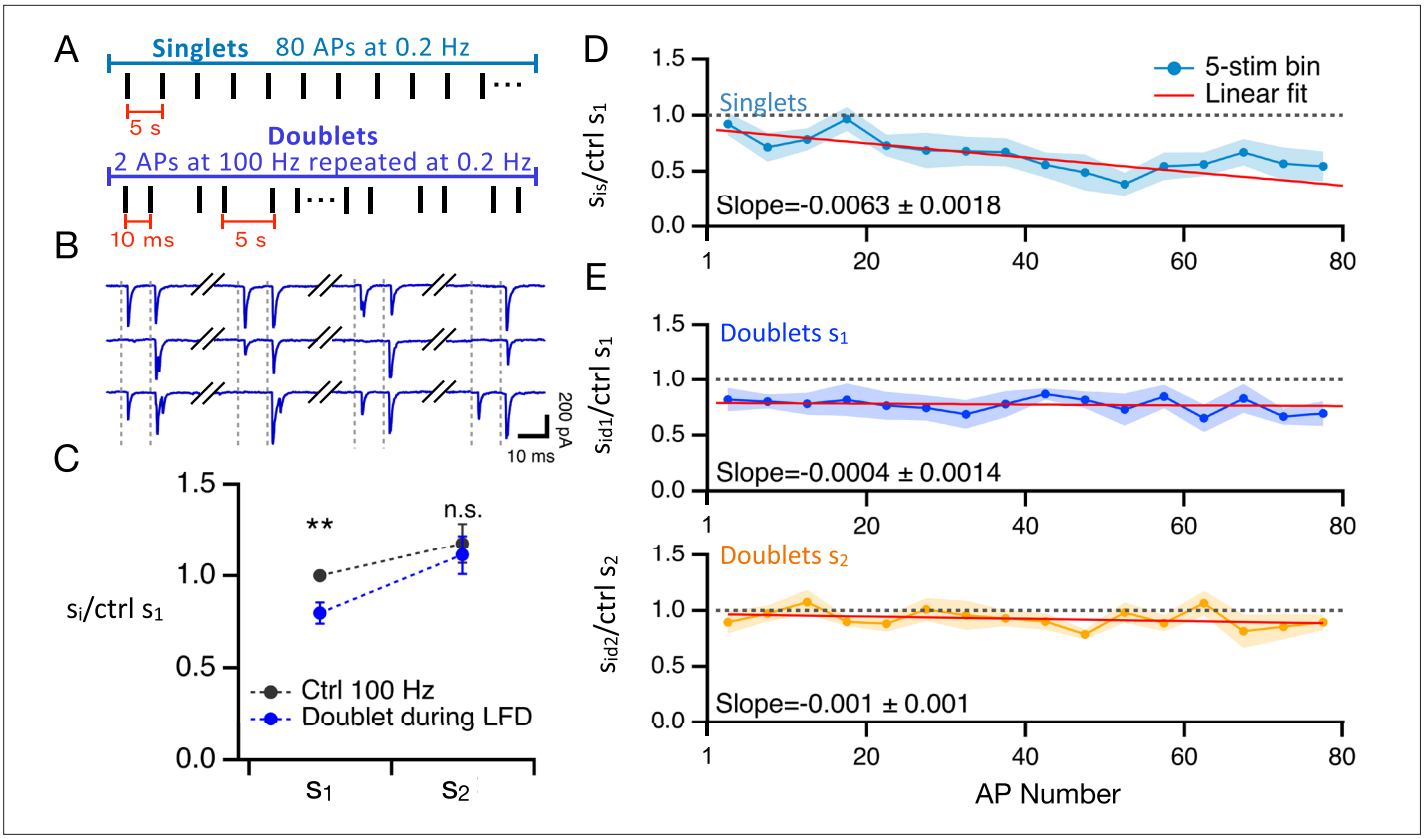


Figure 8. LFD during doublet vs. singlet train stimulations. (**A**) Stimulation protocols. Either an 80-AP train of single stimulations ('singlets') or a sequence of 80 double stimulations 10ms apart ('doublets') were applied at 0.2 Hz. Having two stimuli provides an evaluation of ρ and δ during LFD by comparing release during control and after AP# 1 or AP# 2 during doublets (s_{id1} and s_{id2}, respectively). (**B**) Example traces of a doublet experiment. (**C**) During the first 20 doublet stimulations, the ratio between s_{id1} and ctrl s_1 is <1, indicating a decrease in δ; however, s_{id2} is not significantly different to ctrl s_2 indicating that the occupancy of the replacement sites (ρ) remains the same as control during LFD. (**D**) Normalized plot of s_i during singlet trains (s_{is}) showing a two-component depression (compare to ***Figure 3***). The initial component is followed by a gradual steep depression during the entire train duration (mean ± SEM of individual trials, normalized with respect to the mean s_1 value obtained during preliminary control trains; blue dots and associated error bars: binned data for five consecutive APs; red, linear fit to the data; eight trials from five cells). (**E**) Normalized plot of s_i during doublet trains (mean ± SEM of individual trials, normalized with respect to the mean value obtained during preliminary control trains; dots and associated error bars: binned data for five consecutive APs; red, linear fit to the data; nine trials from six cells). Top: SV release for the first AP of each doublet (s_{id1}) displays a rapid LFD component but no significant slow component. Bottom: SV release for the second AP of each doublet (s_{id2}), showing no significant deviation from the control value.

2nd AP of doublet stimulations (s_{id2}; orange; ***Figure 8D–E***). In each case, the curves could be approximated to linear decay curves as a function of i ($y = \alpha - \beta i$), but the line parameters differed for the three curves. Values of α were similar for s_{id1} and for s_{is} (0.79±0.07 and 0.88±0.11 respectively; p=0.53, two-tailed, two-sample t-test). This indicates that the first phase of LFD occurs with a similar amplitude for singlets and for doublets. On the other hand, values of β were markedly smaller for s_{id1} than for s_{is} (β_{d1} = 0.0004 ± 0.0014 vs. β_s = 0.0063 ± 0.0018; p=0.011, two-tailed, two-sample t-test; ***Figure 8D*** and ***Figure 8E***, *top*). These results suggest that the second phase of LFD is less pronounced for doublet stimulations than for singlet stimulations, with a slope ratio near 15-fold. The results for d_2 can be interpreted as a return of ρ values close to control at the end of each 5 s ISI throughout the train (orange curve in ***Figure 8E***, *bottom*; α_{d2} = 0.97 ± 0.04; β_{d2} = 0.001 ± 0.001), which suggests that the RS gate was closed at the end of each ISI after transitorily opening during the preceding doublet.

Overall, the responses to the first stimulations in doublets display less LFD than singlets, and the responses to the second stimulations in doublets display no LFD at all. The results are consistent with the notion that LFD involves a closing of the RS gate, which is transiently alleviated by doublet stimulations.

Discussion

In the present work, we use the SV counting method at simple PF-MLI synapses (***Malagon et al., 2016***) to investigate cellular mechanisms underlying LFD. Our results reveal similarities, but also significant differences, between these mechanisms and those previously described for moderate- or high-frequency synaptic depression (***Lin et al., 2022***; ***Tran et al., 2022***). Based on our results and on our simulations using the RS/DS model, we propose that LFD reflects a decrease in δ following SV undocking. We also explain how the mechanisms of synaptic depression may vary as a function of stimulation frequency.

PPR as a function of ISI

A traditional view of synaptic physiology has been that synapses may be either facilitating or depressing. This view is clearly an oversimplification, as many synapses display a combination of facilitating and depressing properties (***Dittman et al., 2000***). Here we show that PF-MLI synapses exhibit PPR values >1 for ISI values comprised between 10 and 200ms, and PPR values <1 for ISI values comprised between ~500 ms and ~1500 ms (***Figure 1***). Importantly, the shift from facilitation to depression is apparent not only in group results (***Figure 1D***) but also in individual experiments (***Figure 1C***). A similar mix of facilitation at short ISI and depression at long ISI has been described in several central synapses (***Chiu and Carter, 2024***; ***Doussau et al., 2017***). Following our analysis of simple synapse recordings, and in view of zap-and-freeze results in hippocampal cultures, we propose that facilitation and LFD are linked together in a docking-undocking sequence following AP stimulation (***Kusick et al., 2020***).

SV movements during HFD and LFD

Based on the present study and on earlier work (***Kusick et al., 2020***; ***Miki et al., 2016***; ***Tran et al., 2022***), we propose a global model for HFD and LFD, as outlined in ***Figure 4D***. If an AP train is presented with short ISIs (~10ms), a rapid sequence of release/docking/replenishment occurs (open RS gate). The arrival of a new AP induces forward movement of SVs (from DS to exocytosis, from RS to DS, and from IP to RS). If a docked SV fails to be released, it does not undock because a new SV rapidly occupies the corresponding RS. These events lead to facilitation at first. IP depletion eventually reduces SV influx into the RRP, such that the IP size becomes rate limiting at the end of the train. This accounts for HFD (HFD loop in ***Figure 4D***, green shade). If an AP train is presented with longer ISIs (0.5 s to 5 s), by contrast, release and replenishment are reduced since many DUs have their DS empty and their RS occupied at the time of the AP (closed RS gate). During the closed RS gate period, ρ is ~0.9, so that the entry rate of SVs from the IP into the RRP, which is proportional to (1- ρ), is reduced 10-fold by RS occupation. By comparison, ρ is ~0.5 when the RS gate is open. The larger ρ value results in a net fivefold slower entry rate when the RS gate is closed compared to when it is open. With longer ISIs, SVs move from the RS to the DS after each AP, but they have the time to move back to the RS before the next AP. Therefore, DUs tend to undergo an idle docking/undocking loop without release, leading to LFD (LFD loop in ***Figure 4D***, blue shade).

AP induced docking and undocking happen in overlapping time frames. In ***Figure 1***, the highest amount of docking is seen at ~10ms ISI (it is also present at 5ms: ***Miki et al., 2016***; ***Silva et al., 2024***). Undocking, on the other hand, is maximal more than 1 s after the AP. For ISIs in between, there is a mix of docking and undocking. According to this model, the PPR recovery observed at ISIs of ~200 ms is only apparent because in this period undocking is still ongoing.

When stimulation is switched to high frequency after LFD, SV release recovers within 10 ms to the same level as during high-frequency control trains (***Figure 2D***; ***Figure 6C***). According to the RS/DS model, this happens because the SVs that are in the RS dock with each AP and are still in the DS when a second AP is presented rapidly (HF recovery in ***Figure 4D***, yellow shade). This would explain why the s_2 of a recovery train is equivalent to the control value. If high-frequency stimulation is continued, the synapse will behave identically to a naïve synapse for the remainder of the train (***Figure 2D***; ***Figure 6C***), and it will eventually undergo HFD (***Figure 6B***; HFD loop in ***Figure 4D***, green shade).

It has long been recognized that synaptic activity enhances RRP replenishment (***Neher and Sakaba, 2008***). While a Ca^{2+}-dependent rate of SV entry into the RRP has been invoked as an underlying mechanism, other explanations cannot be ruled out (***Miki et al., 2020***; ***Ritzau-Jost et al., 2018***; ***Ritzau-Jost et al., 2014***). Transient opening of the RS gate, as suggested here, offers a novel mechanism explaining activity-dependent RRP replenishment.

LFD may involve a specific δ decrease rather than across-the-board RRP decrease

Our conclusion that LFD results from a δ decrease is largely based on our analysis of high-frequency recovery trains. While this approach is model-dependent, as it assumes the RS/DS model of ***Figure 2A***, our conclusion is supported by two additional lines of evidence. First, we find that LFD occurs even after failures, and that the extent of LFD does not depend significantly on s_1 (***Figure 5***). These findings argue against the standard RRP depletion mechanism. By contrast, the docking-undocking sequence of ***Figure 4D*** (main sequence and LFD loop) accounts for our results as it predicts that the DU state at the end of a long ISI depends little on the response to the previous stimulation (simulation in ***Figure 5B***). Secondly, we find that LFD is alleviated when using doublet rather than singlet stimulations (***Figure 8***). Again, this result is inconsistent with an across-the-board RRP depletion model, but it can be readily explained by the RS/DS model. During LFD with singlet stimulations, the RS/DS model predicts a gradual δ decrease accompanied by a high ρ (***Figure 3***). Doublet stimulations change this pattern in two ways. Firstly, they transiently lift the RS block that prevents RRP refilling with singlet stimulations, leading to enhanced RRP replenishment. The second AP of the doublet arrives in the period where SVs are still present in the DS, releasing a fraction of them, and promoting SV movement from the RS to the DS. This means that SVs coming from the IP are allowed, in turn, to bind the now-free RS. Secondly, doublet stimulations prevent SV undocking. This happens as the incoming SV at the RS locks the SV that is bound to the DS in its docked position. The combination of these two effects leads to an inhibition of the slow phase of LFD during doublet stimulations. Of note, this complex RS/DS interaction is only possible because the RS/DS model allows simultaneous occupation of both RS and DS by distinct SVs (***Silva et al., 2024***).

Altogether, the present LFD model resembles previous studies assuming two different SV states inside the RRP, and a decrease in the percentage of primed/docked SVs during synaptic depression (***Doussau et al., 2017***; ***Tanaka et al., 2021***; ***Tran et al., 2022***; ***Lin et al., 2025***). It differs from these earlier studies in proposing a role of RS in gating SV movements during LFD.

While our model assumes that the δ decrease associated with LFD is primarily due to the return from DS to RS (undocking), we cannot exclude alternative mechanisms. SVs could leave the DS following exocytosis, or they could unbind and diffuse away in the cytosol. A previous study suggested that delayed release is insufficient to account for the δ decrease accompanying the end of facilitation (***Miki et al., 2018***), making the first option unlikely, but it remains possible that during LFD, part of the δ decrease is due to SV escape into the cytosol independently of the DS->RS transition.

Alternative presynaptic depression mechanisms

Simple synapse recording and deconvolution analysis give us a direct estimate of the number of SVs released, bypassing any possible postsynaptic effects. Expression of LFD as described in the present work is therefore presynaptic. Furthermore, our BAPTA experiments (***Figure 6—figure supplement 3***) argue against a participation of the postsynaptic compartment to LFD induction, so that both induction and expression of LFD are likely presynaptic. We consider here other presynaptic mechanisms than undocking that have been proposed to underlie LFD. A p_r reduction has been suggested (***Wölfel et al., 2007***; ***Wu and Borst, 1999***), either resulting from a direct reduction in Ca^{2+} current (***Xu and Wu, 2005***) or from the buffering effect of calretinin (***Bolshakov et al., 2019***). The rapid reversal obtained during recovery trains in the present work is not consistent with either of these hypotheses, as both Ca^{2+} channel inhibition and a buffering effect would require hundreds of ms to seconds to recover. Furthermore, the results and simulations shown in ***Figure 6F*** suggest a change of δ but not of p_r during LFD. Finally, our Ca^{2+} measurements in presynaptic varicosities do not suggest a difference in Ca^{2+} entry following repetitive low-frequency stimulation, although there is a change in basal calcium during long trains that could be linked to the second, slow phase of LFD (***Figure 7***). Of note, Ca^{2+} measurements have also been performed in relation to LFD in neocortical L4-L2/3 synapses with synaptic depression and no change in Ca^{2+} signal for paired stimuli was reported at ISIs of 500ms (***Chiu and Carter, 2024***). In *Aplysia*, silencing of docking sites was suggested as the reason behind synaptic depression (***Doussau et al., 2010***); however, a decrease in N would not predict the rapid return of high-frequency release when recovery trains are applied after LFD.

In conclusion, it is unlikely that a p_r or N reduction underlies LFD. Overall, a δ reduction best explains LFD and its fast recovery.

Onset and offset kinetics of LFD

In some studies, LFD has been reported to develop almost immediately, after one or a few stimulations (***Chiu and Carter, 2024***; ***Rudolph et al., 2011***), whereas in others it develops much more slowly as a function of stimulation number (***Abrahamsson et al., 2007***; ***Doussau et al., 2017***). In the present work, we observe an immediate reduction in synaptic output (***Figure 2***) followed by a very slow phase which does not reach a steady state after 200 APs at 2 Hz (***Figure 6A***) and 80 APs at 0.2 Hz (***Figure 8D***). After a short train, in which only the initial phase is observed, and after a long train, where both phases are present, we find a reduction in DS occupancy but no changes in RS or IP occupancy (***Figures 2E and 6D***). This leads us to propose that LFD comprises two phases with different onset kinetics.

We find that LFD fails to recover significantly following a rest period of up to 1 min (***Figure 6—figure supplement 1***). These results are consistent with earlier studies showing that for sparse stimulations, LFD recovery occurs on a time scale of minutes (***Abrahamsson et al., 2007***; ***Doussau et al., 2010***; ***Doussau et al., 2017***). If, however, a high-frequency train is presented, the synapse recovers from LFD almost instantaneously, within one single ISI (range 5–20ms ***Doussau et al., 2010***; ***Doussau et al., 2017***; present work, ***Figures 2, 6 and 8***). As seen in ***Figure 4D***, the high-frequency recovery loop after LFD is identical to the HFD loop: presenting new APs at short ISI does not leave enough time for undocking and immediately brings the synapse back to the HFD mode. Altogether, LFD places the synapse in a depressed state that is stable if stimulation is absent or infrequent, but that is immediately reversed if a high-frequency train is presented. In our model, this dichotomy occurs because the SV-RS association is stable at rest, when presynaptic Ca^{2+} concentrations are low (RS gate closed) but is unstable during high-frequency AP trains, when presynaptic Ca^{2+} concentrations are elevated (RS gate open). In contrast to LFD recovery, HFD recovers within seconds following the end of a high-frequency train, reflecting the gradual replenishment of the IP (***Tran et al., 2022***).

Frequency-independent synaptic depression

In the present work, we observe similar extents of LFD at the end of the first phase for stimulation frequencies of 0.2 Hz (0.75±0.11), 1 Hz (0.79±0.08), and 2 Hz (0.69±0.05). These results indicate that at PF-MLI synapses, the first phase of LFD results in a largely frequency-independent steady-state synaptic output in the frequency range 0.2–2Hz. It has been likewise noted in earlier studies that the extent of synaptic depression at steady-state is largely independent of stimulation frequency in a certain frequency range, albeit in a higher range than in the present work (10–100 Hz at Purkinje cell to deep cerebellar nuclei synapses ***Turecek et al., 2016***; 5–50 Hz at the calyx of Held ***Lin et al., 2022***). These results have been interpreted either by a compensation between an increased facilitating component and an increased depressing component at higher frequencies (***Turecek et al., 2017***; ***Turecek et al., 2016***), or by a time limitation on calcium-dependent movement of SVs from a primed to pre-primed location, so that this movement is regulated by AP number rather than by time (***Lin et al., 2025***).

Molecular mechanisms of docking and undocking

The molecular mechanisms of docking and undocking are under intense scrutiny. Consistent with a role in AP-dependent docking, synaptotagmin 7 (syt7) is associated with facilitation in different preparations (***Huson and Regehr, 2020***; ***Jackman et al., 2016***; ***MacDougall et al., 2018***). Using zap-and-freeze electron microscopy in hippocampal cultures revealed that syt7 KO showed no rapid docking ~10 ms after an AP, which was translated into a depressing phenotype when trains of APs are applied (***Wu et al., 2024***). In neocortical synapses, a comparison of PPR curves in wild-type and syt7 KO showed no facilitation at short ISIs and a deeper depression at longer ISIs in the KO, with the same recovery time frame (5 s; ***Chiu and Carter, 2024***), supporting a role of syt7 in AP-dependent docking, but not in undocking or baseline docking dynamics. Recently, intersectin-1 and endophilin A1 were reported to stabilize SVs in the replacement site (RS; ***Ogunmowo et al., 2025***), indicating a role in docking/undocking and possibly in LFD. Munc-13 is another likely candidate for docking (***Kusick et al., 2022***), as its deletion reduces the number of docked SVs and changes their relative distance to the plasma membrane (***Imig et al., 2014***; ***Siksou et al., 2009***). In the calyx of Held, RRP recovery after high-frequency facilitation and depression depends on both Munc13 and synaptotagmin 3 (syt3;

Weingarten et al., 2022). Modeling suggested that both proteins are required to explain AP-dependent docking.

In conclusion, multiple proteins have been proposed as candidates for AP-dependent docking; in our preparation, Munc-13, syt3, and syt7 are likely candidates. By contrast, the molecular mechanisms behind undocking remain largely unknown. It is likely that some of the STP heterogeneity arises from variations in protein expression and regulation among synapses, so that the docking/undocking kinetics are not the same. However, LFD is present in multiple preparations and may be a general mechanism.

Functional implications

In vivo MLI recordings show very infrequent EPSCs in the absence of PF input (<1 Hz), while sensory stimulation results in short EPSC trains at high frequency (*Chadderton et al., 2004*; *Jörntell and Ekerot, 2003*). LFD as described here likely contributes to lower the frequency of background EPSCs, as it inhibits the responses to infrequent presynaptic APs.

However, in view of the rapidity of the post-LFD recovery, full EPSC responses are likely restored as soon as a high-frequency train of presynaptic APs is presented. This should increase the signal-to-noise ratio in a burst vs. background signaling mode and should improve the sensitivity of the cerebellar circuitry to external inputs. As many brain neurons display low background firing rates (<1 Hz) in vivo (*Buzsáki and Mizuseki, 2014*; *Margrie et al., 2002*), a similar signal-to-noise improvement could occur in various brain regions following LFD.

Materials and methods

Experimental model

C57BL/6 mice (12–16 days old; either sex) were used for preparation of acute brain slices. Animals were purchased from Janvier Laboratories (RRID:MGI:2670020). They were housed and cared for in accordance with guidelines of Université Paris Cité (approval no. D 75-06-07; animal rearing service of the BioMedTech Facilities, INSERM US36, CNRS UMS2009).

Slice preparation

200-µm-thick sagittal slices were prepared from the cerebellar vermis as follows. Mice were decapitated under anesthesia and the cerebellar vermis was carefully removed. Dissections were performed in ice-cold artificial cerebrospinal fluid (ACSF) which contained the following (in mM): 130 NaCl, 2.5 KCl, 26 $NaHCO_3$, 1.3 NaH_2PO_4, 10 glucose, 1.5 $CaCl_2$, and 1 $MgCl_2$. Slices were cut using a vibratome (VT1200S; Leica) and incubated in ACSF at 34 °C for at least 60 min before being used for experiments.

Synaptic electrophysiology

Whole-cell patch-clamp recordings were obtained from MLIs (comprising both basket and stellate cells). The extracellular solution contained (in mM): 130 NaCl, 2.5 KCl, 26 $NaHCO_3$, 1.3 NaH_2PO_4, 10 glucose, 3 $CaCl_2$ (1.5 in the experiments where it is stated), and 1 $MgCl_2$ (pH set to 7.4 with 95% O_2 and 5% CO_2). The internal recording solution contained (in mM): 144 K- gluconate, 6 KCl, 4.6 $MgCl_2$, 1 EGTA (ethylene glycol-bis tetraacetic acid), 0.1 $CaCl_2$, 10 HEPES (2-hydroxyethyl)-1-piperazine-eth anesulfonic acid, 4 ATP-Na, 0.4 GTP-Na (pH 7.3, 300 mosm/l). Gabazine (3 µM) was included in all experiments to block $GABA_A$ receptors. Recording temperature was 32–34°C. To establish a single PF–MLI connection, puffs using a glass pipette filled with the high K^+ internal solution were applied in the granule cell layer to identify a potential presynaptic granule cell. The same pipette was then used for extracellular electrical stimulation of the granule cell, with minimal stimulation voltage (stimulus voltage was higher than threshold by ~5 V; range: 10–40 V; 150 µs duration). If the resulting EPSCs, particularly those that occurred after a short stimulation train, were homogeneous, then it was likely that only one presynaptic cell was stimulated. Recordings were only accepted as a simple synapse recording after analysis if the following three criteria were satisfied (*Malagon et al., 2016*): (1) the EPSC amplitude of the second release event in a pair was smaller than that of the first, reflecting activation of a common set of receptors belonging to one postsynaptic density; (2) all the EPSC amplitudes followed a Gaussian distribution with a coefficient of variation <0.5; and (3) the number of release events during the baseline recording was stable.

Quantification and statistical analysis

Offline analysis of electrophysiological data and statistical analysis was performed using Igor Pro (WaveMetrics). Data are expressed as mean ± SEM. Error bars in all graphs indicate SEM. Details of statistical tests are described in the text or figure legends. Student's t-test was used when the distribution was Gaussian; Wilcoxon rank test was used otherwise. One-tailed tests were used when the sign of the effect was predicted before performing the experiments; two-tailed tests were used otherwise. Statistical significance was accepted when $P<0.05$. The number of trials and cells (some cells have multiple trials) for each experiment is indicated by a lowercase n. Cells were derived from different animals. Each experiment started with control recordings of 8-AP trains @ 100 Hz, with 10 s inter-train intervals. At least 25 trials were performed for this initial control run before proceeding to specific stimulation protocols. For PPR experiments (***Figure 1***) 4-AP trains were applied with varying ISIs (20, 100, 200, 400, 800, 1600 and 3200ms) in a scrambled order, with a rest period of 10 s between trains (***Figure 1A*****, right**); only synapses with a minimum of 20 repetitions of this protocol were considered for analysis. For ***Figure 2*** 8-AP trains at alternating frequencies (100 Hz and 2 Hz) were applied. A 100 Hz recovery train was applied immediately after the end of each 2 Hz train (see ***Figure 2B***); a minimum of 20 repetitions of the protocol were obtained for each synapse. Since the value of s_1 should be independent of train frequency (the synapse cannot predict the frequency at which the train will be given), values of s_1 were averaged across frequencies in each synapse. Therefore, in ***Figure 1D***, the s_1 SV # used for calculation of the PPR was averaged across 8 frequencies. In ***Figure 2***, the s_1 value used for normalization is the average of s_1 values for the control 100 Hz train and for the 2 Hz train at each train cycle. For these two protocols, the repetitions of each synapse were averaged together, and synapse results were averaged for group results. For ***Figure 6*** a 200-AP train was applied at low-frequency (2 Hz), followed by a 50-AP or 100-AP high-frequency (100 Hz) recovery train (***Figure 6A***). The time interval between the last AP in the LFD train and the 1st AP in the awakening train varied in the experiments (***Figure 6—figure supplement 1***). Synapses were considered with a minimum of one full trial (low frequency + recovery); the maximum number of trials performed in one synapse was 4. Trials were averaged for group results. For ***Figure 8***, 80 AP trains were applied at 0.2 Hz with either a single or a double stimulus (***Figure 8A***); trials were averaged together for group results. In 5 cells singlets and doublets were applied sequentially. For all protocols, a new control run was performed when possible at the end of the experiment to verify functional stability of the synapse. For each set of experiments, the numbers of repetitions are stated in the figure legend.

Decomposition of EPSCs

The time of occurrence and the amplitude of individual release events were determined based on deconvolution analysis, as described previously (***Malagon et al., 2016***). In brief, for each synapse, an mEPSC (miniature excitatory postsynaptic current) template was obtained from delayed release events recorded after the end of AP trains. This template was fitted with a triple-exponential function with five free parameters (rise time, peak amplitude, fast decay time constant, slow decay time constant, and amplitude fraction of slow decay). These five parameters were then used for deconvolution of the template and of individual data traces, producing a narrow spike (called spike template) and sequences of spikes, respectively. Next, each deconvolved trace was fitted with a sum of scaled versions of the spike template, yielding the timing and amplitude of each release event. The amplitude was further corrected for receptor saturation and desensitization, using the exponential relationship between individual amplitudes and the time interval since the preceding release events. Events that were at least 1.7 times larger than the average mEPSC were split into two (***Miki et al., 2017***). s_1 was determined as the number of SVs released within 5ms after the first AP of a train. s_2 was the number of SVs released within 5ms after the second AP and $s_{5\text{-}8}$ was the cumulative number of SVs released 5 ms after each stimulus for AP# 5–8. As explained (***Tran et al., 2022***), these 3 parameters are proxies respectively for the occupancy of DS (δ), the occupancy of RS (ρ), and the IP size.

Calcium measurements

To perform Ca^{2+} imaging of single PF varicosities we pre-loaded granule cells with a calcium indicator. A whole-cell recording was made with a K^+ gluconate-based solution containing 166 K gluconate, 4.1 $MgCl_2$, 9.9 HEPES-K, 0.36 Na-GTP, and 3.6 Na-ATP, 1–2 mM of the calcium probe Oregon Green BAPTA 6 F. The neurons were held in I-clamp mode with currents of –5 to –30 pA injected to keep

the average resting potential close to –90 mV for 1.5–2 minutes after which the pipette was removed. Obtaining an outside-out patch with >5 GΩ resistance indicated successful pipette removal, and the granule cell was left for approximately 15 minutes to allow for dye diffusion into the axonal compartment. After this waiting time, a 2-photon laser scanning microscope (***Tan et al., 1999***) was used to identify an axonal varicosity. A glass pipette with tip diameter around 1 µm, filled with extracellular saline (in mM: 145 NaCl, 2.5 KCl, 10 K-HEPES, 2 $CaCl_2$, 1 $MgCl_2$), was introduced into the slice at the depth of the varicosity and placed 10–20 µm from the axon. The stimulation protocol consisted of 1 train of 8 pulses (100 µs duration, 10–40 V) delivered at 100 Hz, followed by either 50 stimulations at 1 Hz or 200 at 2 Hz and a new 8 pulse train at 100 Hz applied 30 seconds after the end of the long train. This cycle was performed 3–7 times. Fluorescence was acquired at dwell time of 5ms/frame through raster scans of 5 by 5 µm fields encompassing the axonal varicosity. For each long stimulation train that was applied, we recorded two fluorescence traces. One trace covered the first 5 APs of the train (trace duration: 5 s at 1 Hz stimulation frequency, and 2.5 s at 2 Hz stimulation frequency). We next interrupted laser illumination and scanning (during 40 s at 1 Hz, and during 95 s at 2 Hz) to minimize photobleaching and photodamage. We resumed two-photon imaging near the end of the train, collecting another trace covering the last 5 APs. Time-dependent fluorescence signals were analyzed in the pixels encompassing the varicosity and quantified in terms of changes relative to pre-stimulus values ($\Delta F/F_0$ expressed in %) with software written in the IGOR-Pro programming environment . To avoid possible errors due to tissue movement, focusing was performed twice: just before the first trace, and again before the second trace. To estimate changes in baseline Ca^{2+} concentration, we compared basal fluorescence averages (calculated just before the 1st AP in each trace) for early and late traces across trials for all experiments. This revealed an apparent (non-significant) increase by 4% of the basal fluorescence at 1 Hz stimulation frequency, and a significant 7% increase at 2 Hz stimulation frequency (***Figure 7E1***). In view of this baseline shift (F_{Inc}), the second $\Delta F/F_0$ trace needed a correction. In this trace, the basal fluorescence used to calculate $\Delta F/F_0$ was corrected according to $F_{0corr} = F_{0app} – F_{Inc}$, leading to the relation $\Delta F/F_{0corr} = \Delta F/F_{0app} * (1+F_{Inc} / F_0)$ where $\Delta F/F_{0app}$ and $\Delta F/F_{0corr}$ are the apparent and corrected values of $\Delta F/F_0$ for the late trace, and the ratio F_{Inc}/F_0 is 4% at 1 Hz and 7% at 2 Hz. For each train of stimuli, $\Delta F/F_0$ values were averaged over 5–7 repetitions at each varicosity, and subsequently, data from all varicosities were pooled together to generate the average signal as a function of time from which mean peak values were extracted.

Model and simulation of SV docking and release

Monte Carlo simulation of two-step SV docking and release (***Figure 3***) was performed using Igor Pro as described previously (***Miki et al., 2016***; ***Silva et al., 2024***; ***Tran et al., 2022***). The model is created by assuming a fixed number (N) of docking units (DUs) with 2 binding sites for each DU (RS and DS; ***Figure 2A***), each of which can be empty or occupied by an SV. The probabilities of initial occupancy for DS and RS are δ and ρ , respectively. The probability of SV release after one AP of an occupied DS is p_r. SV transitions within the DU are characterized by transition probabilities s_f, s_b, r_f, r_b.

For each series of experiments, control runs (usually 30 trials) were initially performed with stimulations of 8 APs at 100 Hz, interspersed by 10 s-long rest periods. We used previously developed procedures to determine from these data the parameters N, δ (the mean DS occupancy before the 1st AP), ρ (the mean RS occupancy before the 1st AP), as well as the probabilities s_f, r_f, and p_r, all of which were assumed constant throughout the AP train. In this part of the simulation, the back transitions s_b and r_b were neglected. The simulation yielded the numbers of released SVs (s_i) as a function of AP#. These numbers were calculated as $s_i = N\ \delta_i\ p_r$ where δ_i is the DS occupancy just before AP# i (***Scheuss and Neher, 2001***). Of note, there were some variations from one set of experiments to another regarding these parameters, reflecting differences between synapses (***Table 1***). Similar observations have been made at calyx of Held synapses (***Lin et al., 2025***).

DS and RS replenishment are not independent of each other. A DS can only be filled if an SV is present in the RS, and a downward transition from the RS can only take place if the DS is empty. Likewise, a transition from DS to RS will only happen if the DS is occupied and the RS empty. These considerations are taken into account in the Monte Carlo model. To better understand how the DUs as a whole changed after an AP and during trains, we considered four DU 'states' and we followed them throughout the simulations: DUs were 'full' when both RS and DS were occupied; 'up' when RS was occupied while DS was empty; 'down' when RS was empty while DS was occupied; 'empty' when

both RS and DS were empty (***Figure 3—figure supplement 1***). The initial δ and ρ values were used to estimate the initial DU states, keeping in mind the following relations: (1) δ = %down + %full, (2) ρ = %up + %full, and (3) %down + %up + %full + %empty = 1. The DU state was tracked alongside δ and ρ for each simulated AP.

The first AP was then simulated by releasing from the DS that were occupied (DU states full and down). Release resulted in an increase of % up and a simultaneous fall of % full (***Figure 3—figure supplement 1B*** grey shade).

Below 10ms, rate constants are largely determined by the large amplitude, fast decaying Ca^{2+} signal occurring near voltage-dependent Ca^{2+} channels ('Ca^{2+} nanodomain'). The first 10ms after an AP were simulated with short time intervals (50 μs) while following ρ, δ and the DU states. This time-frame only takes into account forward transitions (r_f and s_f), which were determined from fitting the 100 Hz control data of each dataset, as described before (***Miki et al., 2016***; ***Silva et al., 2024***). This simulation was then used to establish the overall DU changes in the first 10ms following an AP. For example, EE was defined as the probability that a DU that was empty just after release would be again empty 10ms after the AP; EU the probability that a DU that was empty just after release would be up 10ms after the AP, and so forth (***Table 1***). These probabilities were used to simulate the initial 10ms of SV replenishment during an ISI for low frequency train simulations. The first 10ms after release are dominated by the calcium-dependent movement of SVs from the RS to the DS (r_f, 'transient docking') which results in an increase in % down and a decrease in % up (see ***Figure 3—figure supplement 1B***).

After 10ms, the rate constants depend on the low amplitude, slowly decaying Ca^{2+} signals averaged over the entire varicosity ('volume-averaged Ca^{2+}'). To calculate DU state changes at times >10ms after the AP, time intervals for the calculations were changed from 50 μs to 10ms. This change of time interval was justified because SV movements slow down markedly as a function of time since the AP. It resulted in a marked reduction in calculation time. The transition between the two time domains occurring at 10ms explains the slight differences between data and simulation points at 10 vs 20ms in ***Figure 3B***. Whereas transition probabilities were assumed to remain constant during the first 10ms, they were assumed to change for each subsequent 10ms time interval as specified in ***Figure 3—figure supplement 1A***. In this part of the simulation, all transitions were considered, including the back transitions s_b and r_b. Note that the rate r_b has a delay before the start of the time-dependent exponential curve and that s_f remains constant throughout the ISI. Between 10 and 100ms after the AP, up and down state proportions were stable, with a low % empty and up DUs and a high % down and full DUs (***Figure 3—figure supplement 1B***; note time scale change at 10ms). Next, SVs moved from DS to RS (undocking, with rate r_b), resulting in a gradual increase in % up and a decrease in % down (***Figure 3B***). As described in the main text, this movement causes a temporary block of replenishment as ρ is high (RS gate closed). Finally, DUs gradually returned to their basal state on a time scale on the order of 10 s.

To model DU states during AP trains at low frequency, high time resolution modeling at times 0–10ms after each AP (time domain 1) was followed by low time resolution modeling starting at 10ms after the AP and ending at the end of each ISI (time domain 2). Models for consecutive APs were concatenated. For each binding site, the simulation started by attributing a site status to DS and RS. This was done at the beginning of each simulation trial by obtaining a pseudo-random value from the binomial distribution with a mean probability equal to the starting value of δ or ρ, for DS and RS respectively. DU states, δ and ρ were then followed step by step during the entire AP train.

Figure 3—figure supplement 1C depicts the changes in DU state during the simulations of high and low frequency 8-AP trains (***Figure 2*** and ***Figure 4***). The proportion of DUs in each of the full/up/down/empty states is shown alongside ρ and δ just before each AP. During high frequency trains (*left*), an increase in % down (purple continuous curve) at the expense of a decrease in % up (green continuous curve) and % full (orange continuous curve) drives the rise in δ. During low frequency trains (*center*), the trend is the opposite, with undocking causing an increase in the % up (green), mirrored by a reduction in δ. This trend is mainly driven by a drop of % full (orange). DU changes during recovery trains (*right*) reproduce those obtained during control (*left*).

The kinetic parameters were adjusted by hand to find a good fit and to achieve a gradual return to the basal state for long ISIs. The simulation parameter values for the second domain were optimized according to the average release observed in the LFD trains as well as to the awakening train with the final δ and ρ values of the LFD train.

The steady state values of the transition rates in ***Figure 3A*** are heavily constrained by the data within the RS/DS model. By contrast, the time dependent components of r_f, r_b, and s_b, reflecting Ca^{2+}- and time-dependent SV movements, are less strictly constrained, due to the limited set of experimental data on the dependence of LFD on ISI.

The states and occupancies were stored for each simulation trial and averages were obtained at the end of the simulation. For the simulations shown, calculations were done 10,000 times for each ISI and resulting averaged values are displayed.

Our LFD simulations reached steady state after a few APs. They are a good model for the first phase of LFD, but they do not account for the second phase of LFD. Modeling the slow phase of LFD would presumably involve changes in rate constants of the model as a function of AP number; such models fall outside the scope of the present work.

Failure analysis

For this analysis, we focused on the first component of LFD and more specifically, on the value of s_2. Results were taken from experiments with ISIs of 500ms (***Figure 2***), 800ms and 1.6 s (***Figure 1***). The trains were sorted according to whether the 1st AP failed or was successful (***Figure 5A***; failures in purple, successes in black). The ratio of the released SV number after AP# 2 (s_2) and the average of the total released SV number after AP# 1 ($<s_1>$) was calculated for the s_1 failures and for the s_1 successes separately. One synapse had no failures; it was excluded from this analysis. Both traces with successes and failures show depression, as evidenced by a $s_2/<s_1>$ (PPR) lower than 1, indicating that loss of SVs is not the main mechanism of LFD (***Figure 5B*, left**).

This analysis was extended by sorting the trains according to the number of SVs released for s_1. Though the data shows a trend of deeper depression with increased release during the 1st AP, the difference is not significant (***Figure 5B*, right**), indicating again that while release may play a role it is not the main mechanism. Next, we evaluated if the simulations replicated this characteristic feature of the data. The simulation trials were sorted the same way as the data and the PPRs calculated for each case (***Figure 5B***; see black dots). The simulation also shows a significant depression for successful trials, with a somewhat stronger correlation between the amount of depression and the initial s_1 value than experimentally observed. Overall, the simulation reproduces well the results of the experiments.

Binomial analysis and predictions

According to the binomial distribution, the probability that s_i, the number of SVs released after AP number i, equals k is $p(k)=P_i^k\ (1-P_i)^{N-k}\ N!/(k!(N-k)!)$, where P_i is the release probability per docking site ($P_i = \delta_i\ p_r$) and N is the number of docking sites (***Malagon et al., 2016***). The values of N and P were obtained by minimizing the summed squared deviations between the binomial prediction and data. This fitting was carried out for the control s_1 data of the synapses in ***Figure 7***, giving the distribution $p_{ctrl}(k)$. LFD was evaluated in a similar manner, considering each of the stimuli in the train as a separate event. The distributions of released SV numbers for 2 examples of control s_1 data is shown in black lines in ***Figure 6—figure supplement 2A*** and red lines show the LFD data distributions, $p_{LFD}(k)$.

We tested the case of the depression in LFD being the result of an increase in stimulus failures, with a constant probability of release. In this case, the probability of failures during LFD, $p_{LFD}(0)$, would be larger than the control probability of failures, $p_{ctl}(0)$, but the rest of the distribution would retain the same shape for the LFD and control distributions: $p_{LFD}(k) / p_{ctl}(k)$=constant for k=1 to N.

Considering that for each distribution, the sum of p(k) from 0 to N is 1, we obtain:

$p_{LFD}(k)=p_{ctl}(k)\ x\ [1-(p_{LFD}(0)- p_{ctl}(0))/(1- p_{ctl}(0))]$ for k=1 to N.

The dotted blue line in the examples of ***Figure 6—figure supplement 2A*** shows the result of this prediction.

If, instead, LFD was the result of a decrease in probability of release, then the p(k) of the LFD data would follow the distribution: $p_{LFD}(k) = (P_{LFD})^k\ x\ (1 - P_{LFD})^{N-k}\ N!/(k!(N-k)!)$.

where N is the number of DS (assumed to be 5 in the example shown) and P_{LFD} is the P calculated from the LFD distribution: $P_{LFD} = 1 - p_{LFD}(0)^{1/N}$. The dotted purple lines in the examples of ***Figure 6—figure supplement 2A*** show the result of this prediction. The LFD data (red line) was then compared to both predictions. In both examples, the decreased P prediction (purple) is much closer to the data than the prediction for increased stimulus failure (blue). To quantify this difference, residuals were calculated for each point in the plot for both predictions. The group data for the residuals of each

prediction is shown in ***Figure 6—figure supplement 2B*, left**. The right panel depicts the average of the residuals. The prediction of a decrease in P is much closer to the data, compared to the prediction for an increase in the number of stimulus failures.

This analysis shows that an increase in stimulus failures does not account for the distribution of events in the LFD trials and that a decrease in P explains this phenomenon better.

Acknowledgements

We thank Takafumi Miki and Shin-ya Kawaguchi for their help in the modeling. This work was supported by CNRS (UMR 8003), by the European Research Council (Advanced Grant SinSyn to AM), and by Agence Nationale pour la Recherche (Grant PLASTICAZ to AM).

Additional information

Funding

Funder	Grant reference number	Author
Agence Nationale de la Recherche	ANR22 CE91 0013 01	Alain Marty
Agence Nationale de la Recherche	Grant PLASTICAZ	Alain Marty
European Research Council	Advanced Grant SinSyn	Alain Marty

The funders had no role in study design, data collection and interpretation, or the decision to submit the work for publication.

Author contributions

Melissa Silva, Isabel Llano, Data curation, Formal analysis, Investigation, Writing – review and editing; Federico F Trigo, Data curation, Investigation, Writing – review and editing; Alain Marty, Conceptualization, Data curation, Formal analysis, Funding acquisition, Investigation, Methodology, Writing – original draft

Author ORCIDs

Federico F Trigo https://orcid.org/0000-0001-6704-7303
Isabel Llano https://orcid.org/0000-0002-7217-9711
Alain Marty https://orcid.org/0000-0001-6478-6880

Ethics

C57BL/6 mice (12-16 days old; either sex) were used for preparation of acute brain slices. Animals were purchased from Janvier Laboratories (RRID:MGI:2670020). They were housed and cared for in accordance with guidelines of Université Paris Cité (approval no. D 75-06-07; animal rearing service of the BioMedTech Facilities, INSERM US36, CNRS 742 UMS2009).

Peer review material

Version of Record:
Reviewer #1 (Public review): https://doi.org/10.7554/eLife.110329.3.sa1
Reviewer #2 (Public review): https://doi.org/10.7554/eLife.110329.3.sa2
Reviewer #3 (Public review): https://doi.org/10.7554/eLife.110329.3.sa3
Author response https://doi.org/10.7554/eLife.110329.3.sa4

Reviewed preprint v2
Reviewer #1 (Public review): https://doi.org/10.7554/eLife.110329.2.sa3
Reviewer #2 (Public review): https://doi.org/10.7554/eLife.110329.2.sa2
Reviewer #3 (Public review): https://doi.org/10.7554/eLife.110329.2.sa1
Author response: https://doi.org/10.7554/eLife.110329.2.sa0
eLife Assessment https://doi.org/10.7554/eLife.110329.2.sa4

Reviewed preprint v1
Reviewer #1 (Public review): https://doi.org/10.7554/eLife.110329.1.sa3
Reviewer #2 (Public review): https://doi.org/10.7554/eLife.110329.1.sa2
Reviewer #3 (Public review): https://doi.org/10.7554/eLife.110329.1.sa1
Author response: https://doi.org/10.7554/eLife.110329.1.sa0
eLife Assessment https://doi.org/10.7554/eLife.110329.1.sa4

Additional files

Supplementary files

MDAR checklist

Data availability

Data has been deposited at https://figshare.com/s/2283b09a77df95fcd543.

The following dataset was generated:

Author(s)	Year	Dataset title	Dataset URL	Database and Identifier
Silva M, Trigo F, Llano I, Marty A	2026	Dataset for published eLife article: Synaptic vesicle undocking induces low frequency depression. eLife 2026	https://figshare.com/s/2283b09a77df95fcd543	figshare, 2283b09a77df95fcd543

References

Abrahamsson T, Gustafsson B, Hanse E. 2007. Reversible synaptic depression in developing rat CA3 CA1 synapses explained by a novel cycle of AMPA silencing-unsilencing. *Journal of Neurophysiology* **98**:2604–2611. DOI: https://doi.org/10.1152/jn.00602.2007, PMID: 17804578

Atluri PP, Regehr WG. 1998. Delayed release of neurotransmitter from cerebellar granule cells. *The Journal of Neuroscience* **18**:8214–8227. DOI: https://doi.org/10.1523/JNEUROSCI.18-20-08214.1998, PMID: 9763467

Betz WJ. 1970. Depression of transmitter release at the neuromuscular junction of the frog. *The Journal of Physiology* **206**:629–644. DOI: https://doi.org/10.1113/jphysiol.1970.sp009034, PMID: 5498509

Blanchard K, Zorrilla de San Martín J, Marty A, Llano I, Trigo FF. 2020. Differentially poised vesicles underlie fast and slow components of release at single synapses. *The Journal of General Physiology* **152**:e201912523. DOI: https://doi.org/10.1085/jgp.201912523, PMID: 32243497

Bolshakov AP, Kolleker A, Volkova EP, Valiullina-Rakhmatullina F, Kolosov PM, Rozov A. 2019. Overexpression of calretinin enhances short-term synaptic depression. *Frontiers in Cellular Neuroscience* **13**:91. DOI: https://doi.org/10.3389/fncel.2019.00091, PMID: 30930749

Borges-Merjane C, Kim O, Jonas P. 2020. Functional electron microscopy, "Flash and Freeze," of identified cortical synapses in acute brain slices. *Neuron* **105**:992–1006. DOI: https://doi.org/10.1016/j.neuron.2019.12.022, PMID: 31928842

Brenowitz SD, Regehr WG. 2007. Reliability and heterogeneity of calcium signaling at single presynaptic boutons of cerebellar granule cells. *The Journal of Neuroscience* **27**:7888–7898. DOI: https://doi.org/10.1523/JNEUROSCI.1064-07.2007, PMID: 17652580

Buzsáki G, Mizuseki K. 2014. The log-dynamic brain: how skewed distributions affect network operations. *Nature Reviews. Neuroscience* **15**:264–278. DOI: https://doi.org/10.1038/nrn3687, PMID: 24569488

Casado M, Dieudonné S, Ascher P. 2000. Presynaptic N-methyl-D-aspartate receptors at the parallel fiber-Purkinje cell synapse. *PNAS* **97**:11593–11597. DOI: https://doi.org/10.1073/pnas.200354297, PMID: 11016958

Chadderton P, Margrie TW, Häusser M. 2004. Integration of quanta in cerebellar granule cells during sensory processing. *Nature* **428**:856–860. DOI: https://doi.org/10.1038/nature02442, PMID: 15103377

Charlton MP, Smith SJ, Zucker RS. 1982. Role of presynaptic calcium ions and channels in synaptic facilitation and depression at the squid giant synapse. *The Journal of Physiology* **323**:173–193. DOI: https://doi.org/10.1113/jphysiol.1982.sp014067, PMID: 6284915

Chiu DN, Carter BC. 2024. Synaptotagmin 7 Sculpts short-term plasticity at a high probability synapse. *The Journal of Neuroscience* **44**:e1756232023. DOI: https://doi.org/10.1523/JNEUROSCI.1756-23.2023, PMID: 38262726

del Castillo J, Katz B. 1954. Statistical factors involved in neuromuscular facilitation and depression. *The Journal of Physiology* **124**:574–585. DOI: https://doi.org/10.1113/jphysiol.1954.sp005130

Dittman JS, Kreitzer AC, Regehr WG. 2000. Interplay between facilitation, depression, and residual calcium at three presynaptic terminals. *The Journal of Neuroscience* **20**:1374–1385. DOI: https://doi.org/10.1523/JNEUROSCI.20-04-01374.2000, PMID: 10662828

Doussau F, Humeau Y, Benfenati F, Poulain B. 2010. A novel form of presynaptic plasticity based on the fast reactivation of release sites switched off during low-frequency depression. *The Journal of Neuroscience* **30**:16679–16691. DOI: https://doi.org/10.1523/JNEUROSCI.3644-09.2010, PMID: 21148007

Doussau F, Schmidt H, Dorgans K, Valera AM, Poulain B, Isope P. 2017. Frequency-dependent mobilization of heterogeneous pools of synaptic vesicles shapes presynaptic plasticity. *eLife* **6**:e28935. DOI: https://doi.org/10.7554/eLife.28935, PMID: 28990927

Eshra A, Schmidt H, Eilers J, Hallermann S. 2021. Calcium dependence of neurotransmitter release at a high fidelity synapse. *eLife* **10**:e70408. DOI: https://doi.org/10.7554/eLife.70408, PMID: 34612812

Fukaya R, Hirai H, Sakamoto H, Hashimotodani Y, Hirose K, Sakaba T. 2023. Increased vesicle fusion competence underlies long-term potentiation at hippocampal mossy fiber synapses. *Science Advances* **9**:eadd3616. DOI: https://doi.org/10.1126/sciadv.add3616, PMID: 36812326

Huson V, Regehr WG. 2020. Diverse roles of Synaptotagmin-7 in regulating vesicle fusion. *Current Opinion in Neurobiology* **63**:42–52. DOI: https://doi.org/10.1016/j.conb.2020.02.006, PMID: 32278209

Imig C, Min SW, Krinner S, Arancillo M, Rosenmund C, Südhof TC, Rhee J, Brose N, Cooper BH. 2014. The morphological and molecular nature of synaptic vesicle priming at presynaptic active zones. *Neuron* **84**:416–431. DOI: https://doi.org/10.1016/j.neuron.2014.10.009, PMID: 25374362

Jackman SL, Turecek J, Belinsky JE, Regehr WG. 2016. The calcium sensor synaptotagmin 7 is required for synaptic facilitation. *Nature* **529**:88–91. DOI: https://doi.org/10.1038/nature16507, PMID: 26738595

Jörntell H, Ekerot CF. 2003. Receptive field plasticity profoundly alters the cutaneous parallel fiber synaptic input to cerebellar interneurons in vivo. *The Journal of Neuroscience* **23**:9620–9631. DOI: https://doi.org/10.1523/JNEUROSCI.23-29-09620.2003, PMID: 14573542

Kavalali ET. 2006. Synaptic vesicle reuse and its implications. *The Neuroscientist* **12**:57–66. DOI: https://doi.org/10.1177/1073858405281852, PMID: 16394193

Kim O, Okamoto Y, Kaufmann WA, Brose N, Shigemoto R, Jonas P. 2024. Presynaptic cAMP-PKA-mediated potentiation induces reconfiguration of synaptic vesicle pools and channel-vesicle coupling at hippocampal mossy fiber boutons. *PLOS Biology* **22**:e3002879. DOI: https://doi.org/10.1371/journal.pbio.3002879, PMID: 39556620

Kobbersmed JR, Grasskamp AT, Jusyte M, Böhme MA, Ditlevsen S, Sørensen JB, Walter AM. 2020. Rapid regulation of vesicle priming explains synaptic facilitation despite heterogeneous vesicle:Ca2+ channel distances. *eLife* **9**:e51032. DOI: https://doi.org/10.7554/eLife.51032

Koppensteiner P, Bhandari P, Önal C, Borges-Merjane C, Le Monnier E, Nakamura Y, Sadakata T, Sanbo M, Hirabayashi M, Brose N, Jonas P, Shigemoto R. 2022. A two-pool mechanism of vesicle release in medial habenula terminals underlies GABAB receptor-mediated potentiation. *bioRxiv*. DOI: https://doi.org/10.1101/2022.10.28.514202

Kusick GF, Chin M, Raychaudhuri S, Lippmann K, Adula KP, Hujber EJ, Vu T, Davis MW, Jorgensen EM, Watanabe S. 2020. Synaptic vesicles transiently dock to refill release sites. *Nature Neuroscience* **23**:1329–1338. DOI: https://doi.org/10.1038/s41593-020-00716-1, PMID: 32989294

Kusick GF, Ogunmowo TH, Watanabe S. 2022. Transient docking of synaptic vesicles: Implications and mechanisms. *Current Opinion in Neurobiology* **74**:102535. DOI: https://doi.org/10.1016/j.conb.2022.102535, PMID: 35398664

Lin KH, Taschenberger H, Neher E. 2022. A sequential two-step priming scheme reproduces diversity in synaptic strength and short-term plasticity. *PNAS* **119**:2207987119. DOI: https://doi.org/10.1073/pnas.2207987119

Lin K, Ranjan M, Lipstein N, Brose N, Neher E, Taschenberger H. 2025. Number and relative abundance of synaptic vesicles in functionally distinct priming states determine synaptic strength and short-term plasticity. *The Journal of Physiology* **603**:6135–6160. DOI: https://doi.org/10.1113/JP286282

MacDougall DD, Lin Z, Chon NL, Jackman SL, Lin H, Knight JD, Anantharam A. 2018. The high-affinity calcium sensor synaptotagmin-7 serves multiple roles in regulated exocytosis. *The Journal of General Physiology* **150**:783–807. DOI: https://doi.org/10.1085/jgp.201711944, PMID: 29794152

Malagon G, Miki T, Llano I, Neher E, Marty A. 2016. Counting vesicular release events reveals binomial release statistics at single glutamatergic synapses. *The Journal of Neuroscience* **36**:4010–4025. DOI: https://doi.org/10.1523/JNEUROSCI.4352-15.2016

Malagon G, Miki T, Tran V, Gomez LC, Marty A. 2020. Incomplete vesicular docking limits synaptic strength under high release probability conditions. *eLife* **9**:e52137. DOI: https://doi.org/10.7554/eLife.52137, PMID: 32228859

Margrie TW, Brecht M, Sakmann B. 2002. In vivo, low-resistance, whole-cell recordings from neurons in the anaesthetized and awake mammalian brain. *Pflugers Archiv* **444**:491–498. DOI: https://doi.org/10.1007/s00424-002-0831-z, PMID: 12136268

Miki T, Malagon G, Pulido C, Llano I, Neher E, Marty A. 2016. Actin- and myosin-dependent vesicle loading of presynaptic docking sites prior to exocytosis. *Neuron* **91**:808–823. DOI: https://doi.org/10.1016/j.neuron.2016.07.033, PMID: 27537485

Miki T, Kaufmann WA, Malagon G, Gomez L, Tabuchi K, Watanabe M, Shigemoto R, Marty A. 2017. Numbers of presynaptic Ca^{2+} channel clusters match those of functionally defined vesicular docking sites in single central synapses. *PNAS* **114**:E5246–E5255. DOI: https://doi.org/10.1073/pnas.1704470114

Miki T, Nakamura Y, Malagon G, Neher E, Marty A. 2018. Two-component latency distributions indicate two-step vesicular release at simple glutamatergic synapses. *Nature Communications* **9**:3943. DOI: https://doi.org/10.1038/s41467-018-06336-5, PMID: 30258069

Miki T, Midorikawa M, Sakaba T. 2020. Direct imaging of rapid tethering of synaptic vesicles accompanying exocytosis at a fast central synapse. *PNAS* **117**:14493–14502. DOI: https://doi.org/10.1073/pnas.2000265117
Müller M, Goutman JD, Kochubey O, Schneggenburger R. 2010. Interaction between facilitation and depression at a large CNS synapse reveals mechanisms of short-term plasticity. *The Journal of Neuroscience* **30**:2007–2016. DOI: https://doi.org/10.1523/JNEUROSCI.4378-09.2010, PMID: 20147529
Neher E, Sakaba T. 2008. Multiple roles of calcium ions in the regulation of neurotransmitter release. *Neuron* **59**:861–872. DOI: https://doi.org/10.1016/j.neuron.2008.08.019, PMID: 18817727
Neher E. 2015. Merits and limitations of vesicle pool models in view of heterogeneous populations of synaptic vesicles. *Neuron* **87**:1131–1142. DOI: https://doi.org/10.1016/j.neuron.2015.08.038, PMID: 26402599
Neher E, Brose N. 2018. Dynamically primed synaptic vesicle states: key to understand synaptic short-term plasticity. *Neuron* **100**:1283–1291. DOI: https://doi.org/10.1016/j.neuron.2018.11.024, PMID: 30571941
Neher E. 2024. Interpretation of presynaptic phenotypes of synaptic plasticity in terms of a two-step priming process. *The Journal of General Physiology* **156**:e202313454. DOI: https://doi.org/10.1085/jgp.202313454, PMID: 38112713
Ogunmowo TH, Hoffmann C, Patel C, Pepper R, Wang H, Gowrisankaran S, Idel J, Ho A, Raychaudhuri S, Maher BJ, Cooper BH, Milosevic I, Milovanovic D, Watanabe S. 2025. Intersectin and endophilin condensates prime synaptic vesicles for release site replenishment. *Nature Neuroscience* **28**:1649–1662. DOI: https://doi.org/10.1038/s41593-025-02002-4, PMID: 40629141
Pulido C, Marty A. 2018. A two-step docking site model predicting different short-term synaptic plasticity patterns. *Journal of General Physiology* **150**:1107–1124. DOI: https://doi.org/10.1085/jgp.201812072
Rebola N, Reva M, Kirizs T, Szoboszlay M, Lőrincz A, Moneron G, Nusser Z, DiGregorio DA. 2019. Distinct nanoscale calcium channel and synaptic vesicle topographies contribute to the diversity of synaptic function. *Neuron* **104**:693–710. DOI: https://doi.org/10.1016/j.neuron.2019.08.014, PMID: 31558350
Redman RS, Silinsky EM. 1994. ATP released together with acetylcholine as the mediator of neuromuscular depression at frog motor nerve endings. *The Journal of Physiology* **477**:117–127. DOI: https://doi.org/10.1113/jphysiol.1994.sp020176
Regehr WG. 2012. Short-term presynaptic plasticity. *Cold Spring Harbor Perspectives in Biology* **4**:a005702. DOI: https://doi.org/10.1101/cshperspect.a005702, PMID: 22751149
Ritzau-Jost A, Delvendahl I, Rings A, Byczkowicz N, Harada H, Shigemoto R, Hirrlinger J, Eilers J, Hallermann S. 2014. Ultrafast action potentials mediate kilohertz signaling at a central synapse. *Neuron* **84**:152–163. DOI: https://doi.org/10.1016/j.neuron.2014.08.036, PMID: 25220814
Ritzau-Jost A, Jablonski L, Viotti J, Lipstein N, Eilers J, Hallermann S. 2018. Apparent calcium dependence of vesicle recruitment. *The Journal of Physiology* **596**:4693–4707. DOI: https://doi.org/10.1113/JP275911
Rossi DJ, Alford S, Mugnaini E, Slater NT. 1995. Properties of transmission at a giant glutamatergic synapse in cerebellum: the mossy fiber-unipolar brush cell synapse. *Journal of Neurophysiology* **74**:24–42. DOI: https://doi.org/10.1152/jn.1995.74.1.24, PMID: 7472327
Rudolph S, Overstreet-Wadiche L, Wadiche JI. 2011. Desynchronization of multivesicular release enhances Purkinje cell output. *Neuron* **70**:991–1004. DOI: https://doi.org/10.1016/j.neuron.2011.03.029, PMID: 21658590
Saviane C, Savtchenko LP, Raffaelli G, Voronin LL, Cherubini E. 2002. Frequency-dependent shift from paired-pulse facilitation to paired-pulse depression at unitary CA3-CA3 synapses in the rat hippocampus. *The Journal of Physiology* **544**:469–476. DOI: https://doi.org/10.1113/jphysiol.2002.026609, PMID: 12381819
Scheuss V, Neher E. 2001. Estimating synaptic parameters from mean, variance, and covariance in trains of synaptic responses. *Biophysical Journal* **81**:1970–1989. DOI: https://doi.org/10.1016/S0006-3495(01)75848-1, PMID: 11566771
Schmidt H. 2019. Control of presynaptic parallel fiber efficacy by activity-dependent regulation of the number of occupied release sites. *Frontiers in Systems Neuroscience* **13**:30. DOI: https://doi.org/10.3389/fnsys.2019.00030, PMID: 31379524
Siksou L, Varoqueaux F, Pascual O, Triller A, Brose N, Marty S. 2009. A common molecular basis for membrane docking and functional priming of synaptic vesicles. *The European Journal of Neuroscience* **30**:49–56. DOI: https://doi.org/10.1111/j.1460-9568.2009.06811.x, PMID: 19558619
Silva M, Tran V, Marty A. 2021. Calcium-dependent docking of synaptic vesicles. *Trends in Neurosciences* **44**:579–592. DOI: https://doi.org/10.1016/j.tins.2021.04.003, PMID: 34049722
Silva M, Tran V, Marty A. 2024. A maximum of two readily releasable vesicles per docking site at a cerebellar single active zone synapse. *eLife* **12**:RP91087. DOI: https://doi.org/10.7554/eLife.91087, PMID: 38180320
Silverman-Gavrila LB, Orth PMR, Charlton MP. 2005. Phosphorylation-dependent low-frequency depression at phasic synapses of a crayfish motoneuron. *The Journal of Neuroscience* **25**:3168–3180. DOI: https://doi.org/10.1523/JNEUROSCI.4908-04.2005, PMID: 15788774
Soler-Llavina GJ, Sabatini BL. 2006. Synapse-specific plasticity and compartmentalized signaling in cerebellar stellate cells. *Nature Neuroscience* **9**:798–806. DOI: https://doi.org/10.1038/nn1698, PMID: 16680164
Tan YP, Llano I, Hopt A, Würriehausen F, Neher E. 1999. Fast scanning and efficient photodetection in a simple two-photon microscope. *Journal of Neuroscience Methods* **92**:123–135. DOI: https://doi.org/10.1016/s0165-0270(99)00103-x, PMID: 10595710
Tanaka M, Sakaba T, Miki T. 2021. Quantal analysis estimates docking site occupancy determining short-term depression at hippocampal glutamatergic synapses. *The Journal of Physiology* **599**:5301–5327. DOI: https://doi.org/10.1113/JP282235, PMID: 34705277

Taschenberger H, Woehler A, Neher E. 2016. Superpriming of synaptic vesicles as a common basis for intersynapse variability and modulation of synaptic strength. *PNAS* **113**:E4548–E4557. DOI: https://doi.org/10.1073/pnas.1606383113
Tran V, Miki T, Marty A. 2022. Three small vesicular pools in sequence govern synaptic response dynamics during action potential trains. *PNAS* **119**:e2114469119. DOI: https://doi.org/10.1073/pnas.2114469119
Tran V, Silva M, Marty A. 2023. Prioritized docking of synaptic vesicles provided by a rapid recycling pathway. *iScience* **26**:106366. DOI: https://doi.org/10.1016/j.isci.2023.106366, PMID: 37009220
Trommershäuser J, Schneggenburger R, Zippelius A, Neher E. 2003. Heterogeneous presynaptic release probabilities: functional relevance for short-term plasticity. *Biophysical Journal* **84**:1563–1579. DOI: https://doi.org/10.1016/s0006-3495(03)749674
Trussell LO, Zhang S, Raman IM. 1993. Desensitization of AMPA receptors upon multiquantal neurotransmitter release. *Neuron* **10**:1185–1196. DOI: https://doi.org/10.1016/08966273(93)90066-z
Turecek J, Jackman SL, Regehr WG. 2016. Synaptic specializations support frequency-independent purkinje cell output from the cerebellar cortex. *Cell Reports* **17**:3256–3268. DOI: https://doi.org/10.1016/j.celrep.2016.11.081
Turecek J, Jackman SL, Regehr WG. 2017. Synaptotagmin 7 confers frequency invariance onto specialized depressing synapses. *Nature* **551**:503–506. DOI: https://doi.org/10.1038/nature24474
Weingarten DJ, Shrestha A, Juda-Nelson K, Kissiwaa SA, Spruston E, Jackman SL. 2022. Fast resupply of synaptic vesicles requires synaptotagmin-3. *Nature* **611**:320–325. DOI: https://doi.org/10.1038/s41586-022-05337-1
Wölfel M, Lou X, Schneggenburger R. 2007. A mechanism intrinsic to the vesicle fusion machinery determines fast and slow transmitter release at a large CNS synapse. *The Journal of Neuroscience* **27**:3198–3210. DOI: https://doi.org/10.1523/JNEUROSCI.4471-06.2007, PMID: 17376981
Wu LG, Borst JGG. 1999. The reduced release probability of releasable vesicles during recovery from short-term synaptic depression. *Neuron* **23**:821–832. DOI: https://doi.org/10.1016/S0896-6273(01)80039-8
Wu Z, Kusick GF, Berns MMM, Raychaudhuri S, Itoh K, Walter AM, Chapman ER, Watanabe S. 2024. Synaptotagmin 7 docks synaptic vesicles to support facilitation and Doc2α-triggered asynchronous release. *eLife* **12**:RP90632. DOI: https://doi.org/10.7554/eLife.90632, PMID: 38536730
Xu J, Wu LG. 2005. The decrease in the presynaptic calcium current is a major cause of short-term depression at a calyx-type synapse. *Neuron* **46**:633–645. DOI: https://doi.org/10.1016/j.neuron.2005.03.024, PMID: 15944131
Zucker RS, Regehr WG. 2002. Short-term synaptic plasticity. *Annual Review of Physiology* **64**:355–405. DOI: https://doi.org/10.1146/annurev.physiol.64.092501.114547, PMID: 11826273